

DEPARTMENT OF PHYSICS
UNIVERSITY OF JYVÄSKYLÄ
RESEARCH REPORT No. 7/2004

DYNAMICS OF MULTIPHASE FLOWS: LIQUID-PARTICLE SUSPENSIONS AND DROPLET SPREADING

BY
PASI RAISKINMÄKI

Academic Dissertation
for the Degree of
Doctor of Philosophy

*To be presented, by permission of the
Faculty of Mathematics and Science
of the University of Jyväskylä,
for public examination in Auditorium FYS-1 of the
University of Jyväskylä on 15. December 2004
at 12 o'clock noon*



Jyväskylä, Finland
December, 2004

Preface

The work reviewed in this thesis has been carried out during the years 1998-2002 in the Department of Physics at the University of Jyväskylä.

First of all, I would like to thank my supervisors Prof. Jussi Timonen and Prof. Markku Kataja for excellent guidance during these years. I am also grateful to my supervisor Docent Antti Koponen not only for introducing me to the fascinating world of the lattice-Boltzmann method but also because of his help and advice throughout the years. I wish to thank Dr. Juha Merikoski, Dr. Jan Åström and Dr. Amir Shakib-Manesh for their contributions during the preparation of the enclosed articles. Special thanks are due to Mr. Ari Jäsberg, Mr. Jari Hyvälouoma, Dr. Kari Hirvi and Mr. Seismo Malm for a very fruitful collaboration. I am grateful to the former inhabitants of room FL348, and to the staff of the Department of Physics for a very inspiring working atmosphere.

The financial support from the Finnish Center of Technology (TEKES) is gratefully acknowledged.

Finally, I wish to thank my parents and parents-in-law for support and advise. But most of all I want to thank my beloved wife Marja, daughter Emilia and son Eetu-Sameli for your love and support.

Jyväskylä, November 2004

Pasi Raiskinmäki

Abstract

Raiskinmäki, Pasi

Dynamics of multiphase flows: liquid-particle suspensions and droplet spreading

Jyväskylä: University of Jyväskylä, 2004, 152 p.

(Research report/Department of Physics, University of Jyväskylä,

ISSN 0075-465X; 7/2004)

ISBN 951-39-1967-6

diss.

Most fluids that appear in nature as well in numerous applications in industry are multiphase fluids such as liquid-particle suspensions. This thesis considers two typical multiphase systems, a liquid-particle suspension in a (two-dimensional) shear flow and a liquid droplet on a porous surface. These systems are analysed by *ab initio* lattice-Boltzmann simulations.

We analysed the dependence of the viscosity of non-Brownian liquid-particle suspensions on the concentration and shape of the suspended particles, and on the shear rate. We found the viscosity to increase with increasing shear rate. This phenomenon was related to enhanced solid-phase momentum transfer across the system. At least two mechanisms were shown to contribute to the solid-phase momentum transfer: clustering of particles and inertial effects. In shear flow suspended particles form dynamic linear clusters, whose size correlates with the viscosity of the suspension for Reynolds numbers $Re_\gamma \lesssim 1$. For high Reynolds numbers $Re_\gamma > 1$, when the cluster size remains almost constant, viscosity increases due to inertial effects.

In the second system we were interested in the dynamic behaviour of liquid droplet impact on a porous substrate. We could explain, at least qualitatively, how the evolution of the wetted area is controlled by impact velocity, contact angle and surface roughness. We also used in this work a tomographic image of a sample of paper board as the substrate. We determined the volume penetrated by the droplet as a function of time, and compared it with the corresponding result of an analytical capillary model. Based on this comparison, it is evident that our simulations capture relevant mechanisms of the penetration process, and that this process can be understood by a properly formulated capillary theory.

Keywords Multiphase flows, lattice Boltzmann, suspension, rheology, capillary penetration, imbibition.

Author's address	Pasi Raiskinmäki Department of Physics University of Jyväskylä Finland
Supervisors	Professor Jussi Timonen Department of Physics University of Jyväskylä Finland
	Professor Markku Kataja Department of Physics University of Jyväskylä Finland
	Docent Antti Koponen Department of Physics University of Jyväskylä Finland
Reviewers	Professor Mark Martinez Department of Chemical and Biological Engineering University of British Columbia Canada
	Professor Risto Ritala Measurement and Information Technology Tampere University of Technology Finland
Opponent	Professor Alfons Hoekstra Department of Mathematics and Computer Science University of Amsterdam The Netherlands

List of Publications

- I P. RAISKINMÄKI, A. SHAKIB-MANESH, A. KOPONEN, A. JÄSBERG, M. KATAJA, AND J. TIMONEN, *Simulation of Non-spherical Particles Suspended in a Shear Flow*. Comput. Phys. Commun. **129** (2000) 185.
- II A. SHAKIB-MANESH, P. RAISKINMÄKI, A. KOPONEN, M. KATAJA, AND J. TIMONEN, *Shear Stress in a Couette Flow of Liquid-Particle Suspensions*. J. Stat. Phys. **107** (2002) 67.
- III P. RAISKINMÄKI, J. A. ÅSTRÖM, M. KATAJA, M. LATVA-KOKKO, A. KOPONEN, A. JÄSBERG, A. SHAKIB-MANESH AND J. TIMONEN, *Clustering and Viscosity in a Shear Flow of a Particulate Suspension*. Phys. Rev. E **68** (2003) 061403.
- IV P. RAISKINMÄKI, A. KOPONEN, J. MERIKOSKI, AND J. TIMONEN, *Spreading Dynamics of Three-dimensional Droplets by the lattice-Boltzmann Method*. Comput. Mat. Sci. **18** (2000) 7.
- V P. RAISKINMÄKI, A. SHAKIB-MANESH, A. KOPONEN, A. JÄSBERG, J. MERIKOSKI, AND J. TIMONEN, *Lattice-Boltzmann Simulation of Capillary Rise Dynamics*. J. Stat. Phys. **107** (2002) 143.

The author of this thesis has written the first draft of the articles [I, IV, V], and also written selected parts of the article [III]. The author has participated in construction of stress calculation algorithm, and analysis of the numerical results of the article [II]. The author has performed all lattice-Boltzmann simulations of the articles [I, III, IV, V].

Contents

Preface	i
Abstract	iii
List of Publications	v
1 Introduction	1
2 Multiphase flows	3
2.1 Kinetic theory and transport phenomena	3
2.2 Equations of multiphase flow	7
2.2.1 Averaged equations	8
2.2.2 Liquid-particle suspensions	12
2.2.3 Mixture model	15
2.3 Numerical approach to multiphase flows	18
2.3.1 The lattice-Boltzmann method	19
2.3.2 Suspension models	25
2.3.3 Multicomponent and multiphase models	27
3 Viscosity of liquid-particle suspensions in Couette flow	31
3.1 Validation of the implemented methods	31
3.2 Some aspects of viscosity for non-Brownian liquid-particle suspensions	35
3.2.1 Effect of particle shape	35
3.2.2 Effect of shear rate	35
3.2.3 Cluster contribution to the viscosity of liquid-particle suspensions	36
3.2.4 Momentum transfer	46
3.2.5 Solid phase stress	49
4 Liquid droplet on a porous surface	53
4.1 Validation of the implemented method	53
4.2 Simulation results	57
5 Conclusions	67

Chapter 1

Introduction

Most of the fluids that appear in *e.g.* numerous applications in industry and also in nature are multiphase fluids such as liquid-particle suspensions. The term 'multiphase fluids' stands for systems with different substances or different phases of matter (solid, liquid, or gas) in coexistence. Based on experiments and theoretical work, dynamics of single-phase fluids are now quite well understood, excluding however turbulence. This understanding does not extend to multiphase flows due to the complex structures of phase interfaces and interactions between them. Even for a simple case of spherical, homogeneous, solid particles added in a laminar single-fluid flow, interaction terms between the phases (see Section 2.2 below) are complex. For this reason existing theories of multiphase flows, which we briefly introduce in Section 2.2, are restricted to a rather general level. Formulation of specific multiphase equations for a system requires detailed information about the constitutive relations and material parameters of the system. In order to control multiphase processes, understanding the basic mechanisms involved is also essential. To this end, studies of multiphase flows are important.

This thesis considers two different multiphase systems: liquid-particle suspension in a shear flow and liquid droplet on a porous surface. Analysis of these systems is based on mesoscopic lattice-Boltzmann fluid-dynamics simulations.

Viscosity is an important material parameter of liquid-particle suspensions. If a liquid-particle suspension is described as a single-phase 'non-Newtonian' fluid, viscosity includes all its rheological information. In practice, viscosity is measured by common viscometers, and is affected by several variables such as *e.g.* particle concentration, shape of the particles and shear rate. As these parameters may vary locally in the flow, the assumption of a single-phase flow may also break down. An important factor related to this problem, although still quite poorly understood, is thus the microstructure of the suspension, as well as inertial effects in the non-Newtonian (dilatant) behaviour of the suspension. It is evident that one should understand much better the relevant momentum transfer mechanisms which lie behind suspension rheology.

Understanding the behaviour of liquid droplets on porous surfaces is also a

long-standing problem in many applications in industry. One should understand how variations in variables such as contact angle, porosity and impact speed affect the behaviour of the droplet. There is need for analytical models and detailed numerical simulations by new realistic *ab initio* methods. A particularly interesting relatively new method is the lattice-Boltzmann method which has already produced many important results.

The first objective of this thesis is to analyze how such parameters as particle concentration, particle shape and shear rate affect the viscosity of liquid-particle suspensions in general, and in particular how the viscosity is affected by the microstructure of the suspension. These issues are dealt with in Chapter 3. The method of choice for these analyses was *ab initio* numerical simulations by the lattice-Boltzmann method, described in some detail in Chapter 2. The second objective of this thesis is to analyze, with the same methods, how droplets impacted on a porous substrate penetrate the substrate. This is another example of a complicated multiphase problem of fundamental as well as practical importance, and is dealt with in Chapter 4. To begin with, we give, in the beginning of Chapter 2, a brief introduction to the general theoretical background of multiphase flows.

Chapter 2

Multiphase flows

2.1 Kinetic theory and transport phenomena

Within classical kinetic theory of gases, the basic variable to be found is the distribution function

$$f(\mathbf{r}, \mathbf{p}, t) = \frac{dN}{d\mathbf{r} d\mathbf{p}}, \quad (2.1)$$

where dN is the number of particles in volume element $d\mathbf{r}$ around point \mathbf{r} and in the momentum space element $d\mathbf{p}$ around momentum \mathbf{p} . Thus, according to Eq. (2.1), distribution function is the density of particles in the phase space. This distribution function plays a crucial role in kinetic theory because from it all relevant statistical quantities of the gas can be calculated.

Distribution function changes with time, because particles continuously enter and leave phase space volume elements, and collide with each others: the time evolution of the distribution function (of a dilute gas) is governed by the Boltzmann equation [1]

$$\left(\frac{\partial}{\partial t} + \frac{\mathbf{p}}{m} \cdot \nabla_{\mathbf{r}} + \mathbf{F} \cdot \nabla_{\mathbf{p}} \right) f(\mathbf{r}, \mathbf{p}, t) = \left(\frac{\partial f}{\partial t} \right)_{coll}. \quad (2.2)$$

The terms on the left-hand side indicate, respectively, the dependence of the distribution function on time, space (also explicitly related to velocity), and momentum (also explicitly related to external force \mathbf{F} acting on the particles). Here m is the mass of the particles, and the collision term $(\frac{\partial f}{\partial t})_{coll}$ on the right-hand side describes the evolution of the distribution function due to collisions between particles.

The collision term, $(\frac{\partial f}{\partial t})_{coll}$, depends on the form of inter-particle interactions. For a dilute gas where the collisions can be considered to be binary collisions, the collision term takes the form [1]

$$\left(\frac{\partial f}{\partial t} \right)_{coll} = \int d\Omega \int d^3 p_2 \{d\sigma/(d\Omega)\} |\mathbf{v}_1 - \mathbf{v}_2| (f'_1 f'_2 - f_1 f_2), \quad (2.3)$$

where a prime indicates a distribution function after the collision, and \mathbf{v} is particle

velocity. A differential scattering cross section $\{d\sigma/(d\Omega)\}$ is the probability per unit angle that an incident particle is scattered into the angle $d\Omega$, and it may be either calculated or measured. The collision term has a very complicated form even in the case of the simplest gases. Therefore, it is appropriate to replace it by a *phenomenological* term

$$\left(\frac{\partial f}{\partial t}\right)_{coll} \approx -\frac{f - f^{eq}}{\xi}, \quad (2.4)$$

where ξ is a collision time or a relaxation time, and f^{eq} indicates the (local) equilibrium distribution function towards which the distribution function is relaxed. This approach is called the 'relaxation time approximation' [2].

Based on Boltzmann's H theorem it can be shown that, under arbitrary initial conditions, the distribution function approaches monotonically the equilibrium distribution function $f^{eq}(\mathbf{r}, \mathbf{p})$, which is the solution of the Boltzmann transport equation Eq. (2.2) with vanishing intermolecular collision term. Thus, the system will stay at the equilibrium state once it has been reached. Maxwell was able to show that the equilibrium distribution function for dilute gases without external forces is given by

$$f^{eq}(\mathbf{p}) = \frac{n}{(2\pi m k_B T)^{3/2}} e^{-(\mathbf{p}-\mathbf{p}_0)^2/(2mk_B T)}, \quad (2.5)$$

where n is the density of particles, \mathbf{p}_0 is the average particle momentum, and T is temperature. If an external force $\mathbf{F} = -\nabla\phi(\mathbf{r})$ would be present in this dilute gas system, the equilibrium function would be [1]

$$f(\mathbf{r}, \mathbf{p}) = f^{eq}(\mathbf{p}) e^{-\phi(\mathbf{r})/(k_B T(\mathbf{r}))}, \quad (2.6)$$

where $f^{eq}(\mathbf{p})$ is given by Eq. (2.5).

If the system is not in equilibrium its distribution function $f(\mathbf{r}, \mathbf{p}, t)$ will deviate from the Maxwell-Boltzmann distribution Eq. (2.5). In this case transport of conserved quantities takes place due to propagation and collisions of particles. Let $\chi = \chi(\mathbf{r}, \mathbf{p})$ be any quantity of a particle such that

$$\chi_1 + \chi_2 = \chi'_1 + \chi'_2 \quad (2.7)$$

holds true in any binary collision. Here $\chi_1 = \chi(\mathbf{r}_1, \mathbf{p}_1)$, etc. It can be shown that [1]

$$\int d^3 p \chi(\mathbf{r}, \mathbf{p}) \left[\frac{\partial f(\mathbf{r}, \mathbf{p}, t)}{\partial t} \right]_{coll} = 0. \quad (2.8)$$

Thus, multiplying the Boltzmann transport equation (2.2) by χ and integrating over \mathbf{p} , one finds

$$\int d^3 p \chi(\mathbf{r}, \mathbf{p}) \left(\frac{\partial}{\partial t} + \frac{p_i}{m} \frac{\partial}{\partial x_i} + F_i \frac{\partial}{\partial v_i} \right) f(\mathbf{r}, \mathbf{p}, t) = 0. \quad (2.9)$$

The average of any property A of particles is defined by means of the distribution

function f such that

$$\langle A \rangle(\mathbf{r}, t) \equiv \frac{1}{n} \int d^3 p A f(\mathbf{r}, \mathbf{p}, t), \quad (2.10)$$

where $n(\mathbf{r}, t) \equiv \int d^3 p f(\mathbf{r}, \mathbf{p}, t)$. Thus, Eq. (2.9) can be finally written in the form

$$\frac{\partial}{\partial t} \langle n\chi \rangle + \frac{\partial}{\partial x_i} \langle nv_i\chi \rangle - n \langle v_i \frac{\partial \chi}{\partial x_i} \rangle - \frac{n}{m} \langle F_i \frac{\partial \chi}{\partial v_i} \rangle = 0. \quad (2.11)$$

By setting $\chi = m$ in Eq. (2.11) and introducing the mass density $\rho(\mathbf{r}, t) \equiv mn(\mathbf{r}, t)$, the equation for mass conservation with $\mathbf{u}(\mathbf{r}, t) \equiv \langle \mathbf{v} \rangle$ can be expressed as

$$\frac{\partial \rho}{\partial t} + \nabla \cdot (\rho \mathbf{u}) = 0. \quad (2.12)$$

Equation (2.12) is also known as the continuity equation (for a hydrodynamical system).

Setting $\chi = mv_i$ in Eq. (2.11), it is possible to write the equation for momentum conservation in the form

$$\frac{\partial}{\partial t} (\rho \mathbf{u}) + \nabla \cdot (\rho \mathbf{u} \mathbf{u}) = \frac{\rho}{m} \mathbf{F} - \nabla \cdot \vec{\sigma}. \quad (2.13)$$

Here $\vec{\sigma}$ is the stress tensor defined by

$$\sigma_{ij} \equiv \rho \langle (v_i - u_i)(v_j - u_j) \rangle. \quad (2.14)$$

By introducing the momentum density $\mathbf{q} = \rho \mathbf{u}$ (and $\delta = \nabla \cdot \vec{\sigma} + \frac{\rho}{m} \mathbf{F}$), Eq. (2.13) can also be expressed in the form

$$\frac{\partial}{\partial t} \mathbf{q} + \nabla \cdot (\mathbf{q} \mathbf{u}) = \delta, \quad (2.15)$$

where $\mathbf{q} \mathbf{u} \equiv \Pi$ is the momentum flux (tensor). Equation (2.15) has the form of a continuity equation, with an additional source term due to external and internal forces acting on the system. Similarly, one can derive an equation for the conservation of energy (see Ref. [1] for details).

If the system is at its equilibrium state $f(\mathbf{r}, \mathbf{p}, t) = f^{eq}(\mathbf{r}, \mathbf{p})$, $(\frac{\partial f^{eq}}{\partial t})_{coll} = 0$. The stress tensor of Eq. (2.14) will now be [1]

$$\sigma_{ij}^{eq} = \rho (m/2\pi k_B T)^{3/2} \int d^3 v (v_i - u_i)(v_j - u_j) e^{-\frac{m}{2\pi k_B T} |\mathbf{v} - \mathbf{u}|^2} = \delta_{ij} P, \quad (2.16)$$

where

$$P = \frac{1}{3} \rho \left(\frac{m}{2\pi k_B T} \right)^{3/2} \int d^3 U U^2 e^{-\frac{m}{2\pi k_B T} U^2} = nk_B T \quad (2.17)$$

is the local pressure. Here $U = |\mathbf{v} - \mathbf{u}|$. Using $\vec{\sigma} = \vec{\sigma}^{eq}$ in the momentum conservation

equation Eq. (2.15) gives

$$\frac{\partial}{\partial t}(\mathbf{u}) + \mathbf{u} \cdot \nabla \mathbf{u} + \frac{1}{\rho} \nabla P = \frac{\mathbf{F}}{m}. \quad (2.18)$$

This is the Euler equation for a nonviscous flow.

In many practical cases of a fluid flow the system is not in exact equilibrium because the hydrodynamic fields vary locally. The distribution function can then be written as a sum of the equilibrium and a non-equilibrium part, $f = f^{eq} + \delta f$. Here δf is of the order of $\lambda \ll L$, where λ is the mean free path, and L is the characteristic wavelength. Now, the stress tensor is given by (for details see Ref. [1])

$$\sigma_{ij} = \frac{\rho}{n} \int d^3 p (v_i - u_i)(v_j - u_j)(f^{eq} + \delta f) = \delta_{ij}P + \tau_{ij}, \quad (2.19)$$

where the viscous stress tensor τ_{ij} is given by

$$\tau_{ij} = -\frac{\xi \rho m^4}{k_B T n} \Lambda_{kl} \int d^3 U U_i U_j (U_k U_l - \frac{1}{3} \delta_{kl} U^2) f^{eq}. \quad (2.20)$$

Here $\Lambda_{kl} \equiv \frac{1}{2} (\frac{\partial u_k}{\partial x_l} + \frac{\partial u_l}{\partial x_k})$. On the other hand, it is well known that in the hydrodynamic regime, the viscous stress tensor for an isotropic fluid is

$$\tau_{ij} = -2\mu(\Lambda_{ij} - \frac{1}{3} \delta_{ij} \nabla \cdot \mathbf{u}). \quad (2.21)$$

For example, comparing the components τ_{12} of Eqs. (2.20) and (2.21), one finds for the coefficient of Newtonian shear viscosity

$$\mu = -\frac{\xi m^5}{k_B T} \int d^3 U U_1^2 U_2^2 f^{eq} = \xi n k_B T. \quad (2.22)$$

Finally, the total stress tensor has now the form

$$\sigma_{ij} = \delta_{ij}P - 2\mu(\Lambda_{ij} - \frac{1}{3} \delta_{ij} \nabla \cdot \mathbf{u}), \quad (2.23)$$

where the first term on the right-hand side contains the stresses due to pressure, and the second term includes the viscous stresses produced by velocity gradients.

Substituting the stress tensor Eq. (2.23) into the momentum conservation equation Eq. (2.13) (and assuming constant μ), the second basic hydrodynamic equation, the Navier-Stokes equation, can be written as

$$\frac{\partial}{\partial t}(\rho \mathbf{u}) + \nabla \cdot (\rho \mathbf{u} \mathbf{u}) = \frac{\rho}{m} \mathbf{F} - \nabla(P - \frac{\mu}{3} \nabla \cdot \mathbf{u}) + \mu \nabla^2 \mathbf{u}. \quad (2.24)$$

For an incompressible fluid the continuity equation Eq. (2.12), and the Navier-Stokes

equation are given by

$$\nabla \cdot \mathbf{u} = 0, \quad (2.25)$$

$$\frac{\partial}{\partial t} \mathbf{u} + (\mathbf{u} \cdot \nabla) \mathbf{u} = \frac{\mathbf{F}}{m} - \frac{1}{\rho} \nabla P + \nu \nabla^2 \mathbf{u}, \quad (2.26)$$

where $\nu = \mu/\rho$ is the kinematic viscosity of the fluid. These basic hydrodynamic equations can also be derived by considering a small element of fluid (*i.e.* an infinitesimal fixed control volume), and applying Newton's second law to the motion of this element [3].

Equations (2.12) and (2.24) comprise four nonlinear coupled partial differential equations for four unknown variables (P, u_1, u_2 and u_3), as density ρ is a constant for incompressible flow. However, analytical solution of these equations is available only in some special cases. Sometimes these equations can be simplified, as was the case with the Euler equation Eq. (2.18) for a non-viscous flow. In the case of stationary creeping flow, where the left-hand side of the Navier-Stokes equation vanishes, the Stokes equation

$$\nabla P = \mu \nabla^2 \mathbf{u} \quad (2.27)$$

is obtained (in the absence of an external force).

2.2 Equations of multiphase flow

The basic equations of fluid mechanics, the continuity equation Eq. (2.12) and the Navier-Stokes equation Eq. (2.24), were introduced in the previous section for single-phase flow. Evidently, for a multiphase fluid the situation is more complicated. While it is rather straightforward to derive the equations for conservation of mass, momentum and energy for an arbitrary mixture, no generally accepted counterpart of the Navier-Stokes equation have been found for multiphase flows [4]. Using *e.g.* a volume averaging procedure [4], it is however quite possible to derive a set of equations for multiphase flows, which in principle correctly describe the dynamics of any multiphase system. Macroscopically inhomogeneous and dissolved flows such as stratified flow (immiscible fluids separated by identifiable interfaces) and slug flow (large bubbles in a continuous fluid) are not considered here. There are several alternative ways to derive averaged multiphase flow equations such as time averaging and ensemble averaging [5]. The resulting generic form will be similar independent of the method used (different methods may, however, offer slightly different views into the physical interpretation of the various terms that appear in the equations). In the following we consider a system comprised of liquid-particle suspension, shown in Fig. 2.1, which includes a mixture of distinct phases.

2.2.1 Averaged equations

We assume that there exists a characteristic dimension L_p of the individual phase domain at the mesoscopic level such that (microscopic level λ) \ll (mesoscopic level L_p) \ll (averaging volume level L_c) \ll (macroscopic level L_s). The averaging volume

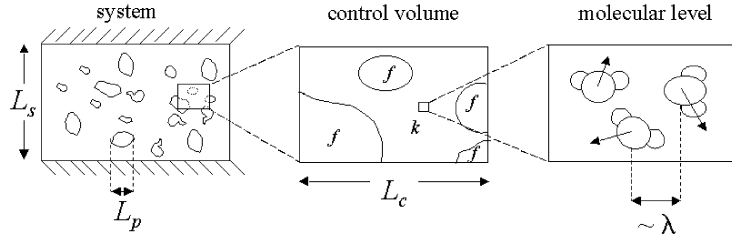


FIGURE 2.1 Characteristic length scales and the control volume used in the continuum approximation.

$V \sim L_c^3$ contains distinct domains of each phase such that $V = \sum_k V_k$, where V_k is the volume of phase k inside V (see Fig. 2.2).

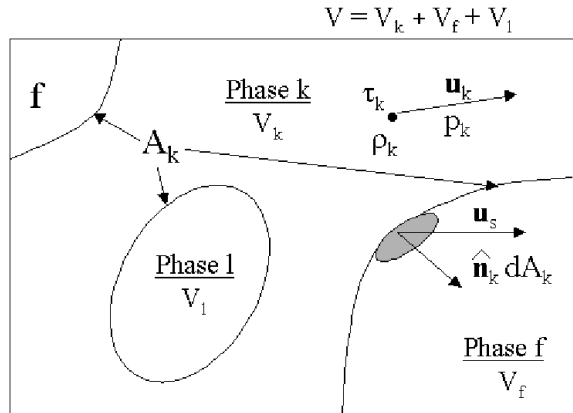


FIGURE 2.2 Averaging volume V including several separated phases.

At any interior point of phase k it is assumed that the equations of mass and momentum conservation are valid in the forms

$$\frac{\partial \rho_k}{\partial t} + \nabla \cdot (\rho_k \mathbf{u}_k) = 0, \quad (2.28)$$

$$\frac{\partial \rho_k \mathbf{u}_k}{\partial t} + \nabla \cdot (\rho_k \mathbf{u}_k \mathbf{u}_k) = \nabla \cdot \vec{\sigma}_k + \mathbf{F}_k. \quad (2.29)$$

Notice that these equations are valid irrespective of whether phase k is fluid or solid material. For fluid, the total stress tensor can be divided into pressure and viscous parts, $\vec{\sigma} = -P\mathbb{I} + \vec{\tau}$. While similar decomposition can be formally made also for solids, it may not be very useful in that case. For solid particles e.g. moving in a

fluid, the local velocity \mathbf{U}_k is, of course, highly correlated inside each particle that moves as a rigid body. (For a derivation of the energy equation for multiphase flows, see e.g. Ref. [4]).

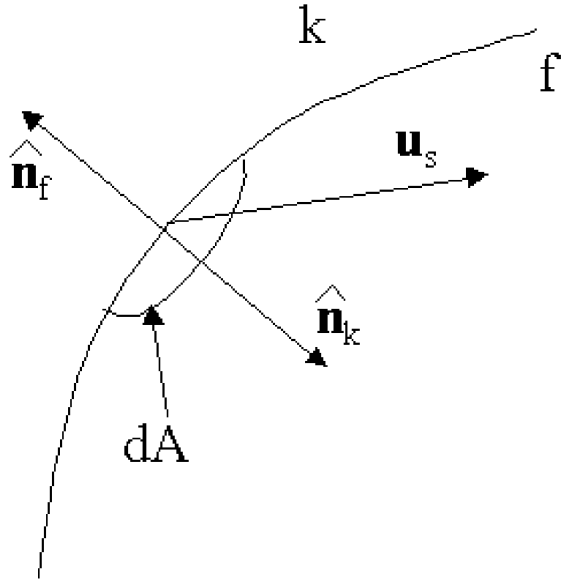


FIGURE 2.3 A position of the interface between phases k and f .

Mass and momentum conservation at an interface A_{kf} between phases k and f (see Fig. 2.3) require that

$$\rho_k(\mathbf{u}_k - \mathbf{u}_s) \cdot \hat{\mathbf{n}}_k + \rho_f(\mathbf{u}_f - \mathbf{u}_s) \cdot \hat{\mathbf{n}}_f = 0, \quad (2.30)$$

and

$$\rho_k \mathbf{u}_k (\mathbf{u}_k - \mathbf{u}_s) \cdot \hat{\mathbf{n}}_k + \rho_f \mathbf{u}_f (\mathbf{u}_f - \mathbf{u}_s) \cdot \hat{\mathbf{n}}_f = (\vec{\sigma}_k) \cdot \hat{\mathbf{n}}_k + (\vec{\sigma}_f) \cdot \hat{\mathbf{n}}_f - \nabla_s \gamma_{kf} + \frac{2\gamma_{kf}}{R_s} \hat{\mathbf{n}}. \quad (2.31)$$

Here, $\hat{\mathbf{n}}_{k,f}$ is the unit outward normal of phase k (f), \mathbf{u}_s the velocity of the interface, R_s the radial interface curvature vector, $\hat{\mathbf{n}} = \mathbf{R}_s/R_s$ ($= \pm \hat{\mathbf{n}}_k; \hat{\mathbf{n}}_k = -\hat{\mathbf{n}}_f$), γ_{kf} the surface tension at the interface, and $\nabla_s = (\nabla - \hat{\mathbf{n}} \cdot \nabla)$ the surface gradient operator. These interface equations Eqs. (2.30) and (2.31) give boundary conditions for the mesoscopic equations of motion Eqs. (2.28) and (2.29). (In addition, it is necessary to apply boundary conditions for each phase separately at the boundary of the physical system.) In practice, the boundary conditions may be very complicated due to the complex shapes of the interface which, in addition, may depend on time. Therefore, it is not usually feasible to numerically solve the mesoscopic equations Eqs. (2.28) and (2.29), with proper boundary conditions (see, however, Section 2.3.1).

For any mesoscopic quantity q_k (scalar, vector or tensor) related to phase k in

the averaging volume V , we define the averaged quantities

$$\langle q_k \rangle = \frac{1}{V} \int_{V_k} q_k dV \quad (2.32)$$

$$\tilde{q}_k = \frac{1}{V_k} \int_{V_k} q_k dV = \frac{1}{\phi_k} \langle q_k \rangle \quad (2.33)$$

$$\bar{q}_k = \frac{\int_{V_k} \rho_k q_k dV}{\int_{V_k} \rho_k dV} = \frac{\langle \rho_k q_k \rangle}{\phi_k \tilde{\rho}_k}, \quad (2.34)$$

where $\phi_k = V_k/V$ is the volume ratio of phase k and $\sum_k \phi_k = 1$. The quantities $\langle q_k \rangle$, \tilde{q}_k and \bar{q}_k given by Eqs. (2.32), (2.33) and (2.34) are called the partial average, the phase average and the mass weighted average of q_k , respectively. We next turn to deriving the governing equations (flow equations) for the various averaged quantities each defined as partial-, phase- or mass-weighted average of the corresponding mesoscopic quantity. (It will become evident in the course of derivation, which averaging is most appropriate for each of the relevant quantities.) The derivation can be done by applying averaging to the phase equations Eqs. (2.28) and (2.29). To do so we have to deal with averages of derivatives. It is straightforward to show that partial averages of various derivatives of any quantity q_k can be given as sums of the corresponding derivatives of a partial average of q_k and additional surface integrals [4],

$$\langle \nabla q_k \rangle = \nabla \langle q_k \rangle + \frac{1}{V} \int_{A_k} q_k \hat{\mathbf{n}}_k dA \quad (2.35)$$

$$\langle \nabla \cdot \mathbf{q}_k \rangle = \nabla \cdot \langle \mathbf{q}_k \rangle + \frac{1}{V} \int_{A_k} \mathbf{q}_k \cdot \hat{\mathbf{n}}_k dA \quad (2.36)$$

$$\langle \frac{\partial}{\partial t} q_k \rangle = \frac{\partial}{\partial t} \langle q_k \rangle - \frac{1}{V} \int_{A_k} q_k \mathbf{u}_s \cdot \hat{\mathbf{n}}_k dA. \quad (2.37)$$

Taking partial average of both sides of Eqs. (2.28) and (2.29) and using Eqs. (2.35)-(2.37), we obtain for the equations of motion

$$\frac{\partial}{\partial t} \langle \rho_k \rangle + \nabla \cdot \langle \rho_k \mathbf{u}_k \rangle = \Gamma_k \quad (2.38)$$

$$\frac{\partial}{\partial t} \langle \rho_k \mathbf{u}_k \rangle + \nabla \cdot \langle \rho_k \mathbf{u}_k \mathbf{u}_k \rangle = -\nabla \langle P_k \rangle + \nabla \cdot \langle \tau_k \rangle + \langle \mathbf{F}_k \rangle + \mathbf{M}_k. \quad (2.39)$$

(For the averaged energy equation, see Ref. [4]). In the above equations Eqs. (2.38) and (2.39), Γ_k and \mathbf{M}_k are the so called 'transfer integrals' given by

$$\Gamma_k = -\frac{1}{V} \int_{A_k} \rho_k (\mathbf{u}_k - \mathbf{u}_s) \cdot \hat{\mathbf{n}}_k \quad (2.40)$$

$$\mathbf{M}_k = \frac{1}{V} \int_{A_k} (\vec{\sigma}_k) \cdot \hat{\mathbf{n}}_k dA - \frac{1}{V} \int_{A_k} \rho_k \mathbf{u}_k (\mathbf{u}_k - \mathbf{u}_s) \cdot \hat{\mathbf{n}}_k dA. \quad (2.41)$$

These transfer integrals describe the interfacial interactions, *i.e.* transfer of mass and momentum from one phase to the others through phase surfaces. This transfer may *e.g.* be due to chemical reactions, phase transitions or work done by the internal stresses. Using Eqs. (2.30) and (2.31), it is easy to see that the transfer integrals Eqs. (2.40) and (2.41) obey the constraints

$$\sum_k \Gamma_k = 0 \quad (2.42)$$

and

$$\sum_k \mathbf{M}_k = -\frac{1}{2V} \sum_{\substack{k,f \\ k \neq f}} \int_{A_{kf}} (-\nabla_s \gamma_{kf} + \frac{2\gamma_{kf}}{R_s} \hat{\mathbf{n}}) dA. \quad (2.43)$$

Equation (2.42) ensures conservation of the total mass of the mixture, while the right-hand side of Eq. (2.43) gives rise to surface effects such as 'capillary' pressure differences between various phases. If the surface tension between the phases is insignificant, the right-hand side of Eq. (2.43) vanishes.

Transfer integrals are still given as surface integrals of the original microscopic quantities over the unknown phase boundaries, and cannot be used in this form. Therefore, transfer integrals must ultimately be replaced by new terms which have the same physical content, but which are given in closed form in terms of the basic averaged quantities. Derivation of such constitutive relations for the transfer integrals is one of the basic problems of multiphase-flow dynamics. No general method to solve that problem exists, because the solution is particular to each system [6]. However, by making a simplified model of the system or with suitable assumptions, it may be possible to estimate these relations. Dimensional analysis and experiments can also be used to find the relevant parameters of the constitutive relations.

As stated above, our goal here is to derive equations that contain averages of phase quantities such as *e.g.* ρ_k and u_k . Equations (2.38) and (2.39) contain, however, averages of products of such quantities, and in general these differ from products of averages of the corresponding variables. Therefore, even in the case that the terms $\langle \mathbf{F}_k \rangle$, $\langle \vec{\sigma}_k \rangle$, Γ_k and \mathbf{M}_k were known, there would still be more independent variables than equations for each phase in the system, *i.e.* the set of equations is not closed. Therefore it is necessary to reduce the number of independent variables by replacing the averages of products by products of suitable averages. To do this we first define the velocity fluctuation $\delta \mathbf{u}_k$ as

$$\delta \mathbf{u}_k \equiv \mathbf{u}_k - \mathbf{V}_k, \quad (2.44)$$

where $\mathbf{V}_k (\equiv \frac{\langle \rho_k \mathbf{u}_k \rangle}{\langle \rho_k \rangle})$ is the mass averaged velocity (Eq. (2.34)). The following closure

relations can then be easily obtained:

$$\langle \rho_k \mathbf{u}_k \rangle = \langle \rho_k \rangle \mathbf{V}_k = \phi_k \tilde{\rho}_k \mathbf{V}_k, \quad (2.45)$$

$$\langle \rho_k \mathbf{u}_k \mathbf{u}_k \rangle = \langle \rho_k \rangle \mathbf{V}_k \mathbf{V}_k + \vec{\tau}_{\delta k} = \phi_k \tilde{\rho}_k \mathbf{V}_k \mathbf{V}_k + \vec{\tau}_{\delta k}. \quad (2.46)$$

Here $\vec{\tau}_{\delta k} = -\langle \rho_k \delta \mathbf{u}_k \delta \mathbf{u}_k \rangle$. Note that $\vec{\tau}_{\delta k}$ has the same form as Reynold's stress tensor in the momentum conservation equation for turbulent single-phase flow. (The standard definition of Reynolds stress involves, however, time averaging rather than volume averaging.) The 'final' equations of motion can be finally expressed in the form

$$\frac{\partial}{\partial t} (\phi_k \tilde{\rho}_k) + \nabla \cdot (\phi_k \tilde{\rho}_k \mathbf{V}_k) = \Gamma_k \quad (2.47)$$

for conservation of mass, and

$$\frac{\partial}{\partial t} (\phi_k \tilde{\rho}_k \mathbf{V}_k) + \nabla \cdot (\phi_k \tilde{\rho}_k \mathbf{V}_k \mathbf{V}_k) = \nabla \cdot \langle \vec{\sigma}_k \rangle + \langle \mathbf{F}_k \rangle + \mathbf{M}_k + \nabla \cdot \vec{\tau}_{\delta k} \quad (2.48)$$

for conservation of momentum. In the same way one could derive the equations for energy and entropy. In the following, a dense liquid-particle suspension is considered as an example where all hydrodynamic quantities are expressed as functions of ρ_k and \mathbf{V}_k .

2.2.2 Liquid-particle suspensions

Consider a binary system of particles suspended in a Newtonian liquid. The liquid phase and the solid phase are denoted by subscript f and s , respectively. We assume that there is no mass transfer between the phases and also neglect the surface tension, and hence find that

$$\Gamma_f = \Gamma_s = 0, \quad (2.49)$$

$$\mathbf{M}_k = \frac{1}{V} \int_{A_k} \vec{\sigma}_k \cdot \hat{\mathbf{n}}_k dA; \quad k = f, s, \quad (2.50)$$

$$\mathbf{M} \equiv \mathbf{M}_f = -\mathbf{M}_s. \quad (2.51)$$

For dense systems where both phases are incompressible, interactions between suspended particles are noticeable. Therefore the stresses in the solid phase differ from those in the fluid phase.

By introducing a phase indicator function Θ_k such that

$$\Theta_f(\mathbf{r}) = \begin{cases} 1, & \mathbf{r} \in V_f, \\ 0, & \text{otherwise,} \end{cases}$$

we find that

$$\langle \Theta_f \rangle = \frac{1}{V} \int_{V_f} \Theta_f dV = \frac{1}{V} V_f = \phi_f \equiv \phi. \quad (2.52)$$

Using Eq. (2.35) with $q_k = \Theta_f$, it can be shown that

$$\frac{1}{V} \int_{A_f} \hat{n} dA = -\nabla \phi. \quad (2.53)$$

Supposing that the pressure fluctuations in the liquid are small within an averaging volume, and using Eq. (2.53), the momentum transfer integral can be expressed in the form

$$\mathbf{M} = \tilde{P}_f \nabla \phi + \mathbf{D}, \quad (2.54)$$

where

$$\mathbf{D} = \frac{1}{V} \int_{A_f} \vec{\tau}_f \cdot \hat{n} dA. \quad (2.55)$$

Transfer integral \mathbf{D} includes momentum transfer due to viscous stresses acting on the surfaces of the particles.

The averaged flow equations can now be expressed in their final form,

$$\frac{\partial}{\partial t} \phi + \nabla \cdot (\phi \mathbf{V}_f) = 0, \quad (2.56)$$

$$\frac{\partial}{\partial t} (1 - \phi) + \nabla \cdot ((1 - \phi) \mathbf{V}_s) = 0, \quad (2.57)$$

$$\begin{aligned} & \tilde{\rho}_f \left(\frac{\partial}{\partial t} (\phi \mathbf{V}_f) + \nabla \cdot (\phi \mathbf{V}_f \mathbf{V}_f) \right) \\ &= -\phi \nabla \tilde{P}_f + \nabla \cdot \langle \vec{\tau}_f \rangle + \phi \tilde{\mathbf{F}}_f + \mathbf{D} + \tilde{\rho}_f \nabla \cdot \vec{\Pi}_f, \end{aligned} \quad (2.58)$$

and

$$\begin{aligned} & \tilde{\rho}_s \left(\frac{\partial}{\partial t} ((1 - \phi) \mathbf{V}_s) + \nabla \cdot ((1 - \phi) \mathbf{V}_s \mathbf{V}_s) \right) \\ &= -(1 - \phi) \nabla \cdot \langle \sigma_s \rangle + (1 - \phi) \tilde{\mathbf{F}}_s - \mathbf{D} - \tilde{P}_f \nabla \phi + \tilde{\rho}_s \nabla \cdot \vec{\Pi}_s, \end{aligned} \quad (2.59)$$

where $\langle \vec{\tau}_f \rangle$ is the averaged viscous stress tensor of the fluid and $\langle \sigma_s \rangle$ is the averaged total stress tensor of the dispersed phase. $\vec{\Pi}_f$ includes the possible turbulent motion of the fluid as well as its 'pseudoturbulent' motion due to the presence of particles. The constitutive relation for the viscous stress tensor $\langle \vec{\tau}_f \rangle$ of an incompressible fluid is normally written as

$$\langle \vec{\tau}_f \rangle = \phi \mu (\nabla \mathbf{V}_f + (\nabla \mathbf{V}_f)^T). \quad (2.60)$$

The stress states inside the particles are determined by the hydrodynamic forces ex-

erted on the surfaces of the particles by the surrounding fluid, and by the collisions between particles. Therefore, the stress tensor $\langle \sigma_s \rangle$ can be very complicated. If the collisions between particles can be ignored (this assumption is adequate for dilute suspensions), and if the velocity difference between the particles and the fluid is small, the constitutive relation for the stress tensor of the particles can be expressed in the form

$$\begin{aligned}\langle \sigma_s \rangle &= (1 - \phi) \tilde{\sigma}_s \\ &\approx (1 - \phi) \tilde{P}_f \mathbb{I}.\end{aligned}\quad (2.61)$$

The transfer integral ('drag term') \mathbf{D} in Eq. (2.55) can be written (based on the work by Drew [5,7]) as

$$\begin{aligned}\mathbf{D} &= a_1(\mathbf{V}_f - \mathbf{V}_s) + a_2 \frac{\partial}{\partial t}(\mathbf{V}_f - \mathbf{V}_s) \\ &+ a_3(\mathbf{V}_f - \mathbf{V}_s) \cdot \frac{1}{2}((\nabla \mathbf{V}_f) + (\nabla \mathbf{V}_f)^T) +\end{aligned}\quad (2.62)$$

Here a_i ($i = 1, 2, \dots$) are unknown but typically measurable parameters.

The first term in Eq. (2.62) is the Stokes drag force. For very dilute suspensions of spherical particles of diameter d and for low Reynolds numbers ($Re = \frac{\tilde{\rho}_f |\mathbf{V}_f - \mathbf{V}_s| d}{\mu_f} < 1$), parameter a_1 is given by

$$a_1 = \frac{3}{4}(1 - \phi) \frac{\mu_f}{d^2} C_D(Re, \phi) Re,\quad (2.63)$$

where the drag coefficient is $C_D \approx \frac{24}{Re}$.

The second term in Eq. (2.62) is called the added mass which arises since accelerating a particle immersed in a fluid accelerates some fluid around the particle as well. It is suggested in Ref. [5] (and in references therein) that

$$a_2 = (1 - \phi) \tilde{\rho}_f C_{AM},\quad (2.64)$$

where $C_{AM} = \frac{1}{2} + \mathcal{O}(1 - \phi)$.

The third term in Eq. (2.62) is a 'lift' force. If a particle is moving e.g. near a solid wall (*i.e.* in a strong environment with velocity gradient), it may experience a lift force which tries to move the particle towards or away from the wall. (Lift force is perpendicular to $\mathbf{V}_f - \mathbf{V}_s$). This may cause *e.g.* a particle-free lubrication layer to be formed near the wall in a pipe flow of a particulate suspension [8]. In addition, many other interactions and mechanisms than those included in Eq. (2.62) may be crucial in practical flow situations of fluid-particle suspensions [5].

The multiphase equations discussed in the preceding section were given in a very general form. Application of these equations demands *e.g.* knowledge of the transfer integral \mathbf{D} . However, for a dense fluid-particle suspension, it is difficult

to find the interaction terms experimentally or analytically. For this reason, maybe the most commonly used approach is to treat multi-component mixtures as single-phase non-Newtonian fluids with given prescribed rheological properties. If it can be assumed that the velocity difference between the phases is small, and if the interfacial interactions can be adequately described by means of rheological variables such as viscosity, this kind of mixture model can be used as an alternative formulation of the problem.

2.2.3 Mixture model

Consider a mixture of two phases and assume that one of the phases is a continuous fluid, and that the second phase is composed of dispersed solid particles. Also, the influence of the surface tension is assumed to be insignificant. In this approach both the continuity equation and the momentum equation are written for a mixture of the continuous and dispersed phases. The complete derivation of the mixture model can be found in Ref. [9] and references therein. The continuity equation for the mixture can be obtained by summing Eq. (2.47) over all phases. Here ρ_m is the mixture density defined as

$$\rho_m = \sum_{\alpha=1}^2 \phi_\alpha \tilde{\rho}_\alpha, \quad (2.65)$$

which can vary although the component densities $\tilde{\rho}_\alpha$ are constant. The mixture velocity $\bar{\mathbf{u}}_m$ is defined as the centre-of-mass velocity,

$$\bar{\mathbf{u}}_m = \frac{1}{\rho_m} \sum_{\alpha=1}^2 \phi_\alpha \tilde{\rho}_\alpha \tilde{\mathbf{u}}_\alpha. \quad (2.66)$$

The continuity equation for the mixture can now be obtained by summing Eq. (2.47) over all phases, and we find that

$$\frac{\partial}{\partial t}(\rho_m) + \nabla \cdot (\rho_m \bar{\mathbf{u}}_m) = 0. \quad (2.67)$$

In the same way the momentum equation can be written in terms of mixture variables, and, consequently,

$$\frac{\partial}{\partial t}(\rho_m \bar{\mathbf{u}}_m) + \nabla \cdot (\rho_m \bar{\mathbf{u}}_m \bar{\mathbf{u}}_m) = -\nabla P_m + \nabla \cdot (\vec{\tau}_m + \vec{\tau}_{\delta m} + \vec{\tau}_{Dm}) + \mathbf{F}_m. \quad (2.68)$$

Here the tensors $\vec{\tau}_m$, $\vec{\tau}_{\delta m}$ and $\vec{\tau}_{Dm}$ are defined as

$$\vec{\tau}_m = - \sum_{\alpha=1}^2 \phi_\alpha \tilde{\tau}_\alpha, \quad (2.69)$$

$$\vec{\tau}_{\delta m} = - \sum_{\alpha=1}^2 \phi_\alpha \langle \tilde{\rho}_\alpha \delta \mathbf{u}_\alpha \delta \mathbf{u}_\alpha \rangle \quad (2.70)$$

and

$$\vec{\tau}_{Dm} = - \sum_{\alpha=1}^2 \phi_\alpha \tilde{\rho}_\alpha \bar{\mathbf{u}}_{m\alpha} \bar{\mathbf{u}}_{m\alpha}. \quad (2.71)$$

They represent the average viscous stress, turbulent stress, and diffusion stress due to the phase slip, respectively. Here diffusion velocity $\bar{\mathbf{u}}_{m\alpha}$ is the velocity of phase α relative to the centre of the mixture mass,

$$\bar{\mathbf{u}}_{m\alpha} = \bar{\mathbf{u}}_\alpha - \bar{\mathbf{u}}_m. \quad (2.72)$$

The term $\nabla \cdot \vec{\tau}_{Dm}$ describes the momentum transfer due to the relative motions of the phases. Usually the phase pressures are supposed to be equal, *i.e.* $\tilde{P}_\alpha = P_m$.

The complete mixture model consists now of Eqs. (2.67) and (2.68), and the constitutive equations for viscous and turbulent stresses. The most simple, but widely used approximation for the viscous stress tensor is to assume that stress tensor is proportional to the strain-rate tensor (this expression is similar to the one used for the viscous stress tensor of an incompressible single-phase fluid),

$$\tau_m = \mu_m [\nabla \bar{\mathbf{u}}_m + (\nabla \bar{\mathbf{u}}_m)^T]. \quad (2.73)$$

In Eq.(2.73) the coefficient of proportionality μ_m is the apparent viscosity of the suspension. It is not necessarily a well defined property of the mixture. It depends on many factors such as fluid-velocity gradient, concentration, particle shape, particle-size distribution, particle-particle interactions, and properties of the suspending liquid. For a dilute dispersed suspension, a famous relation was derived by Einstein [10]:

$$\mu_m = \mu_f (1 + 2.5\phi_s). \quad (2.74)$$

Here μ_f is the viscosity of the suspending fluid. Equation (2.74) neglects all other factors but concentration, because theory is based on the assumptions that particles do not interact hydrodynamically, and Brownian motion of the particles is insignificant. When the effects of interactions between the particles are included, the situation becomes more complicated. The inclusion of hydrodynamic two-particle interactions *e.g.* leads to a 2nd-order term in ϕ_s . In this case the apparent viscosity of a dilute suspension can be written as [11]

$$\mu_m = \mu_f (1 + 2.5\phi_s + k_2\phi_s^2). \quad (2.75)$$

For shear flows the value of coefficient k_2 has been experimentally found to vary between 5 and 15. This fairly large interval of possible k_2 values implies that this co-

efficient depends on many factors such as the shear rate $\dot{\gamma}$. Dilute-suspension theory is applicable only for low concentrations ($\phi_s < 10\%$) which are not realised in many practical applications.

When extending the dilute-suspension analysis to higher concentrations, difficulties arise in computing the many-body hydrodynamic interactions, and in finding the microscopic configurations of the suspension. A simple and frequently used expression for the apparent viscosity μ_m is the (semi-empirical) Krieger-Dougherty relation [12]

$$\mu_m = \mu_f \left(1 - \frac{\phi_s}{\phi_{\max}}\right)^{-[\eta]\phi_{\max}}, \quad (2.76)$$

where ϕ_{\max} is the concentration at maximal packing density, *i.e.* at the concentration at which the suspension 'jams'. In a jammed state the particle phase percolates through the system. This makes flow impossible, and the apparent viscosity diverges. Even for suspensions of ideal spherical particles the maximum packing densities may vary between 0.50 (for simple cubic packing $\phi_{\max} = 0.52$) and 0.75 (for hexagonal close packing $\phi_{\max} = 0.74$), depending on the microscopic structure of the particle phase (for random close packing $\phi_{\max} \approx 0.63$). For example, particle flocculation or nonspherical shape of particles may decrease the maximum packing density. On the other hand, suspensions with a distribution of particle sizes have higher ϕ_{\max} [13]. In practical applications the size distribution is continuous, and information about ϕ_{\max} is not usually available in the literature. The factor $[\eta]$ in Eq. (2.76) is the so-called intrinsic viscosity which depends on the shape and charge of the particles. For spherical non-charged particles $[\eta] = 2.5$. Note that the value of the coefficient in Einstein relation Eq. (2.74) remains the same.

As mentioned before, the apparent viscosity μ_m is a function of shear rate $\dot{\gamma}$. The generic form of this dependence on μ_m is shown in Fig. 2.4 [13].

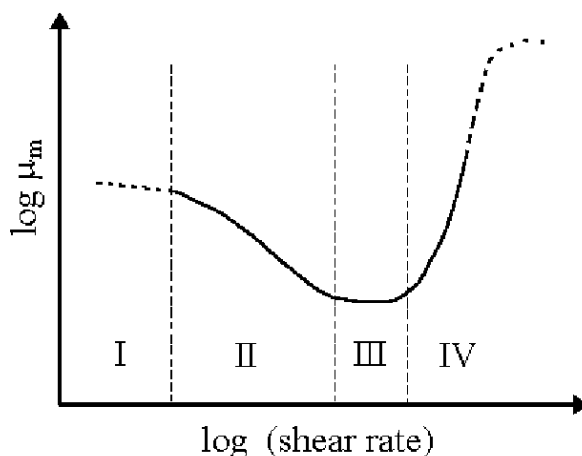


FIGURE 2.4 The generic behaviour of the apparent viscosity of a liquid-particle suspension as a function of shear rate.

The first Newtonian plateau ($\mu_m \approx \text{constant}$) appears at low shear rates, where Brownian motion dominates over the other motions of the particles (Region I in Fig. 2.4). The structure of the particle phase is approximately random, and when the suspension flows, the particles have to move around each other. This causes a relatively high apparent viscosity. Increasing shear rate decreases the disorder of the particle structure (Region II in Fig. 2.4). This can be seen as a lower apparent viscosity. In this regime suspension displays shear-thinning. A second Newtonian plateau follows the shear thinning region (Region III in Fig. 2.4). In this regime the apparent viscosity assumes its lowest value, and particles are strongly orientated [13]. They may form layers separated by a fluid phase. When the shear rate is still increased, the layers will be dissolved [14], and particles may form substructures such as clusters (or flocs) that are deformed by the shear force [15, 16, 17]. The capability of the particles to transfer momentum still increases for increasing shear rates, as interactions between suspended particles and the surrounding fluid become stronger due to hydrodynamic instabilities (an inertial effect). This leads to increasing apparent viscosity, *i.e.* suspension displays shear-thickening (Region IV in Fig. 2.4).

For non-Newtonian fluids a commonly used relation between μ_m and the shear rate $\dot{\gamma}$ is a *power law* of the form

$$\mu_m(\dot{\gamma}) = K\dot{\gamma}^{n-1}, \quad (2.77)$$

with two experimentally determined parameters are K and n . For $n < 1$, Eq. (2.77) describes the viscosity of a shear-thinning fluid (Region II in Fig. 2.4). On the other hand, the viscosity of a shear-thickening, or *dilatant*, fluid is found for $n > 1$ (Region IV in Fig. 2.4). For $n = 1$, the fluid behaves as a Newtonian fluid, and $K = \mu_m$. So, parameter K is related to the magnitude of viscosity.

2.3 Numerical approach to multiphase flows

In the previous two sections (2.1) and (2.2) equations for conservation of mass and momentum in multiphase flows (Eqs. (2.47) and (2.48)) were derived starting from kinetic theory. As already pointed out, equations for multiphase flows are very complicated mainly due to complex boundary conditions. Therefore, analytical solution of these equations is generally impossible. Previously, experiments provided the only feasible way to study multiphase flows. Continuous development of computing power has, however, made numerical simulations an attractive and practical way to solve these multiphase equations. These can be roughly divided into three categories according to the characteristic length scale of the method used.

Macroscopic simulations are traditionally related to finding a direct mathematical solution to macroscopic continuum equations for fluid flow. The basic idea behind these computational fluid dynamic (CFD) [3] simulations is to discretize, *e.g.*,

the mass and momentum conservation equations Eqs. (2.47) and (2.48), and then solve these discretized equations with proper initial and boundary conditions using an appropriate numerical algorithm. However, the problem of obtaining the constitutive relations and the material laws still remains in various CFD methods. For this reason CFD simulations are limited to certain applications (cf. Section 2.2.3).

Fluid-flow problems could in principle be solved at the microscopic (atomic) level with direct molecular-dynamical (MD) simulations. This approach would, however, require enormous computational resources as the number of molecules needed to represent the liquid phase of a dilute particle suspension is huge.

Difficulties in obtaining the constitutive relations may be avoided by using mesoscale simulation techniques developed during the last two decades such as the lattice-gas automata (LGA) [18], its derivative the lattice-Boltzmann method (LBM) [19] or the dissipative particle dynamics (DPD) method [20, 21]. Instead of solving the macroscopic continuum equations or tracking individual molecules, these methods are based on a mesoscopic approach to hydrodynamics.

In this section the lattice-Boltzmann method (LBM), the lattice-BGK model in particular, and its extension to multiphase flows will briefly be introduced [22, 23, 24, 25].

2.3.1 The lattice-Boltzmann method

The lattice-Boltzmann method is based on the lattice-gas automata (LGA) which belong to the family of cellular automata (CA). Richard Feynman suggested that the idea behind LGA can be explained as follows: "*We have noticed in nature that the behaviour of a fluid depends very little on the nature of individual particles in that fluid. For example, the flow of sand is very similar to the flow of water or the flow of a pile of ball bearings. We have therefore taken advantage of this fact to invent a type of imaginary particle that is especially simple for us to simulate. This particle is a perfect ball bearing that can move at a single speed in one of six directions. The flow of these particles on a large enough scale is very similar to the flow of natural fluids.*" (Quoted by Rothman and Zaleski in Ref. [24].) In LGA a realistically behaving fluid model can be constructed from discrete identical particles which move in a discrete lattice. In addition to space, also time and particle velocities are discrete. Basically, the fluid particles move during each time step from a lattice node to one of its nearest neighbours. However, at the lattice nodes particles are not allowed to have identical velocities. After the propagation phase particles interact locally such that particle velocities are reshuffled while mass and momentum are conserved (collision phase). Frisch, Hasslacher and Pomeau originally showed in Ref. [18] that LGA implemented on a hexagonal lattice leads to the Navies-Stokes equation in the continuum limit.

The lattice-Boltzmann (LB) model has evolved from lattice-gas models by replacing the particle with a distribution function $f_i(\mathbf{r}, t)$ that gives the probability of

finding a particle at site \mathbf{r} at time t going in the \mathbf{c}_i direction. Thus, the dynamics of LBM is described by a discrete lattice-Boltzmann equation (LBE) [18, 19],

$$f_i(\mathbf{r} + \mathbf{c}_i, t + 1) - f_i(\mathbf{r}, t) = \Omega_i(\mathbf{r}, t), \quad (2.78)$$

where $\Omega_i(\mathbf{r}, t)$ is a collision operator. The main requirement of the collision operator is that it must satisfy conservation of mass,

$$\sum_{i=0}^N \Omega_i(\mathbf{r}, t) = 0, \quad (2.79)$$

and conservation of momentum,

$$\sum_{i=0}^N \Omega_i(\mathbf{r}, t) \mathbf{c}_i = 0. \quad (2.80)$$

As in kinetic theory the collision operator can be simplified by making the relaxation-time approximation:

$$\Omega_i = -\frac{1}{\xi}(f_i(\mathbf{r}, t) - f_i^{eq}(\mathbf{r}, t)), \quad (2.81)$$

where ξ is a relaxation-time parameter. Here $f_i^{eq}(\mathbf{r}, t)$ is the equilibrium distribution towards which the particle populations are relaxed. This is called the BGK (Bhatnager, Gross and Krook) approximation in kinetic theory (see Eq. (2.4)) [2]. By applying Eq. (2.81) in Eq. (2.78), an equation of evolution for the lattice-BGK model [26, 27] is obtained,

$$f_i(\mathbf{r} + \mathbf{c}_i, t + 1) = f_i(\mathbf{r}, t) + \frac{1}{\xi}[f_i^{eq}(\mathbf{r}, t) - f_i(\mathbf{r}, t)]. \quad (2.82)$$

The lattice-BGK model is the simplest of the lattice-Boltzmann models. For a detailed derivation of the lattice-Boltzmann equation Eq. (2.78) from kinetic theory, see e.g. Refs. [28, 29, 30]. In equilibrium,

$$\sum_{i=0}^N f_i^{eq}(\mathbf{r} + \mathbf{c}_i, t + 1) = \sum_{i=0}^N f_i^{eq}(\mathbf{r}, t). \quad (2.83)$$

The local equilibrium distribution can be written in the form of a second-order expansion in velocity of the local Maxwellian distribution (in the limit of small velocities or low Mach numbers):

$$f_i^{eq} = w_i \rho \left(1 + \frac{1}{c_s^2} (\mathbf{c}_i \cdot \mathbf{u}) + \frac{1}{c_s^4} (\mathbf{c}_i \cdot \mathbf{u})^2 - \frac{1}{2c_s^2} u^2 \right), \quad (2.84)$$

in which w_i is a weight factor. The weight factors should be chosen in such a way that the required fluid properties are obtained. For example, in hydrodynamics the

total stress tensor is isotropic. For this reason the weight factors w_i should be chosen such that this isotropy requirement is fulfilled. Thus, for any cubic lattice

$$\sum_{i=0}^N w_i c_{i\alpha} c_{i\beta} = K_2 \delta_{\alpha\beta}, \quad (2.85)$$

and

$$\sum_{i=0}^N w_i c_{i\alpha} c_{i\beta} c_{i\gamma} c_{i\delta} = K_4 (\delta_{\alpha\beta}\delta_{\gamma\delta} + \delta_{\alpha\gamma}\delta_{\beta\delta} + \delta_{\alpha\delta}\delta_{\beta\gamma}), \quad (2.86)$$

where K_2 and K_4 are numerical coefficients that depend on the choice of the weights, and $\delta_{\alpha\beta}$ is the Kronecker delta function. Similar sums with odd numbers of velocity components $c_{i\alpha}$, should vanish. Here the greek letters label the spatial components of the velocity vectors. In addition to being isotropic, a proper simulation model should also be Galilean invariant [24, 31].

Two typical simulation lattices are the D_2Q_9 lattice in 2D and the D_3Q_{19} lattice in 3D. Here d in D_d refers to the dimension of the problem, and N in Q_N to the number of different discrete velocities (links) in the model. In these lattices the lengths of the links are $|\mathbf{c}_0| = 0$, $|\mathbf{c}_1| = 1$, $|\mathbf{c}_2| = \sqrt{2}$ for the rest particles, and the particles that move along the nearest-neighbour and next-nearest-neighbour links, respectively. Figure 2.5 illustrates the lattices and links.

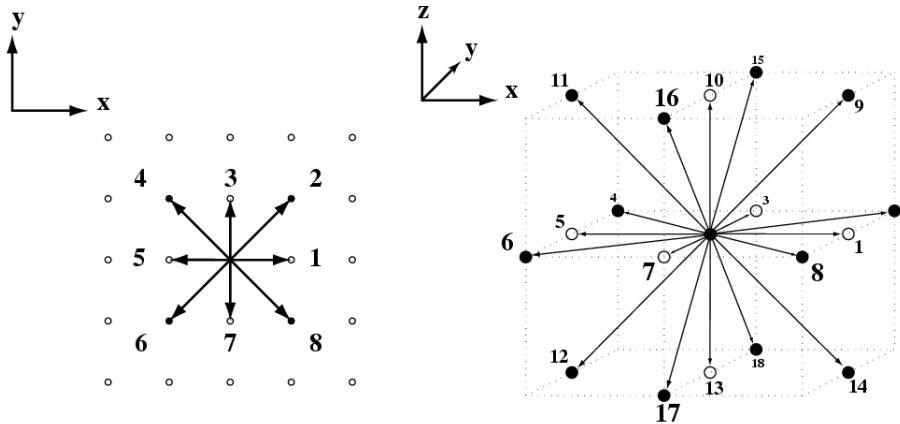


FIGURE 2.5 The lattice structures of the D_2Q_9 and the D_3Q_{19} lattice-BGK models.

One choice for the weight factors of these lattices, which fulfill the requirements listed above, is $w_0 = 4/9$, $w_1 = 1/9$, and $w_2 = 1/36$ for the D_2Q_9 lattice, and $w_0 = 1/3$, $w_1 = 1/18$, and $w_2 = 1/36$ for the D_3Q_{19} lattice [26]. With these choices the K coefficients become $K_2 \equiv (c_s)^2 = 1/3$, and $K_4 \equiv (c_s)^4 = 1/9$, where c_s is the speed of sound.

The basic hydrodynamic variables are obtained in the lattice-Boltzmann model from the velocity moments in analogy with kinetic theory. The density ρ , the flow

velocity \mathbf{u} , and the fluid-momentum-flux tensor $\vec{\Pi}$ are given, respectively, by

$$\rho(\mathbf{r}, t) = \sum_{i=0}^N f_i(\mathbf{r}, t) \quad (2.87)$$

$$\rho(\mathbf{r}, t)\mathbf{u}(\mathbf{r}, t) = \sum_{i=1}^N \mathbf{c}_i f_i(\mathbf{r}, t) \quad (2.88)$$

$$\vec{\Pi}(\mathbf{r}, t) = \sum_{i=1}^N \mathbf{c}_i \mathbf{c}_i f_i(\mathbf{r}, t). \quad (2.89)$$

The convection tensor,

$$\vec{\mathbf{C}}(\mathbf{r}, t) = \rho(\mathbf{r}, t)\mathbf{u}(\mathbf{r}, t)\mathbf{u}(\mathbf{r}, t), \quad (2.90)$$

can be directly calculated from density ρ and velocity \mathbf{u} , and the viscous stress tensor $\vec{\mathbf{M}}$ is given by

$$\vec{\mathbf{M}}(\mathbf{r}, t) = \vec{\Pi}(\mathbf{r}, t) - \vec{\mathbf{C}}(\mathbf{r}, t). \quad (2.91)$$

The conservation equations in LBM can be derived by using a Chapman-Enskog expansion [31, 18]. The first step is to make a Taylor expansion of Eq. (2.78),

$$f_i(\mathbf{r} + \mathbf{c}_i, t+1) - f_i(\mathbf{r}, t) \simeq [\partial_t + c_{i\alpha} \partial_\alpha + \frac{1}{2} c_{i\alpha} \partial_\alpha (c_{i\beta} \partial_\beta + \partial_t) + \frac{1}{2} \partial_t (c_{i\alpha} \partial_\alpha + \partial_t)] f_i(\mathbf{r}, t), \quad (2.92)$$

and then expand the distribution function, and time and space derivatives such that

$$\begin{aligned} f_i &= f_i^{eq} + \epsilon f_i^{(1)} + \epsilon^2 f_i^{(2)} \dots, \\ \partial_t &= \epsilon \partial_{1t} + \epsilon^2 \partial_{2t} + \dots, \\ \partial_r &= \epsilon \partial_{1r}, \end{aligned} \quad (2.93)$$

where f_i^{eq} is the equilibrium distribution function defined in Eq. (2.84), and $\epsilon f_i^{(1)} + \epsilon^2 f_i^{(2)} + \dots$ indicate the nonequilibrium part of the distribution. In Eq. (2.93) it is assumed that the diffusion time scale t_2 is much smaller than the convection time scale t_1 . The Chapman-Enskog equation can now be derived by using the above equations, *i.e.*, by substituting Eq. (2.93) into equations (2.78), (2.81) and (2.92). From Eq. (2.92) we obtain

$$\partial_{1t} f_i^{eq} + \partial_{1\alpha} c_{i\alpha} f_i^{eq} = -\frac{1}{\xi} f_i^{(1)} \quad (2.94)$$

to first order in ϵ , and

$$[\partial_{1t} + \partial_{1\alpha} c_{i\alpha}] f_i^{(1)} + [\partial_{2t} + \frac{1}{2} (\partial_{1t} + \partial_{1\alpha} c_{i\alpha})^2] f_i^{eq} = -\frac{1}{\xi} f_i^{(2)} \quad (2.95)$$

to second order in ϵ . Substituting Eq. (2.94) into Eq. (2.95), we find

$$\partial_{2t} f_i^{eq} + (\partial_{1t} + \partial_{1\alpha} c_{i\alpha}) (1 - \frac{1}{2\xi}) f_i^{(1)} = -\frac{1}{\xi} f_i^{(2)}. \quad (2.96)$$

Summing over i on both sides of Eq. (2.94), we obtain the mass conservation equation

$$\frac{\partial \rho}{\partial t} + \nabla \cdot (\rho \mathbf{u}) = 0. \quad (2.97)$$

Multiplying by $c_{i\beta}$ and summing over i on both sides of Eqs. (2.94) and (2.95), and then combining them, we obtain the momentum conservation equation

$$\frac{\partial(\rho \mathbf{u})}{\partial t} + \nabla \cdot \vec{\Pi} = 0, \quad (2.98)$$

where the momentum-flux tensor $\vec{\Pi}$ has the form

$$\begin{aligned} \Pi_{\alpha\beta} &= \Pi_{\alpha\beta}^{(eq)} + \Pi_{\alpha\beta}^{(1)} \\ &= \sum_{i=1}^N c_{i\alpha} c_{i\beta} [f_i^{eq} + (1 - \frac{1}{2\xi}) f_i^{(1)}]. \end{aligned} \quad (2.99)$$

Inserting the equilibrium distribution of Eq. (2.84) with the coefficients given above into Eq. (2.99), we find

$$\begin{aligned} \Pi_{\alpha\beta}^{(eq)} &= \sum_{i=1}^N c_{i\alpha} c_{i\beta} f_i^{eq} = p \delta_{\alpha\beta} + \rho u_\alpha u_\beta \\ \Pi_{\alpha\beta}^{(1)} &= \left(1 - \frac{1}{2\xi}\right) \sum_{i=1}^N c_{i\alpha} c_{i\beta} f_i^{(1)} = \nu (\partial_\alpha (\rho u_\beta) + \partial_\beta (\rho u_\alpha)), \end{aligned} \quad (2.100)$$

where

$$p(\mathbf{r}, t) = c_s^2 (\rho(\mathbf{r}, t) - \rho_f) \quad (2.101)$$

is fluid pressure with the average fluid density ρ_f . Now the sound velocity is $c_s = 1/\sqrt{3}$, and the kinematic viscosity is $\nu = (2\xi - 1)/6$. We can thus write the resulting momentum equation for an incompressible fluid with constant density in the form

$$\frac{\partial \mathbf{u}}{\partial t} + (\mathbf{u} \cdot \nabla) \mathbf{u} = -\frac{1}{\rho} \nabla p + \nu \nabla^2 \mathbf{u}, \quad (2.102)$$

which is the usual Navier-Stokes equation in the continuum limit. The boundary condition between the fluid and a solid wall is the no-slip condition, *i.e.* the velocity of the fluid at the wall must be the same as the velocity of the wall. The no-slip boundary condition in the LBM is usually realised by the bounce-back rule [32]. This means simply that the populations f_i pointing towards a wall (\mathbf{c}_i) are simply

reversed ($\mathbf{c}_i \rightarrow -\mathbf{c}_i$) at a collision. The bounce-back boundary condition is very easy to implement in LBM. This makes LBM attractive for simulating *e.g.* particulate suspensions. Bounce-back can be applied either at nodes (Bounce-Back on Nodes, BBN) or at halfway between the fluid and solid points (Bounce-Back on Links, BBL). Figure 2.6 illustrates these bounce-back rules.

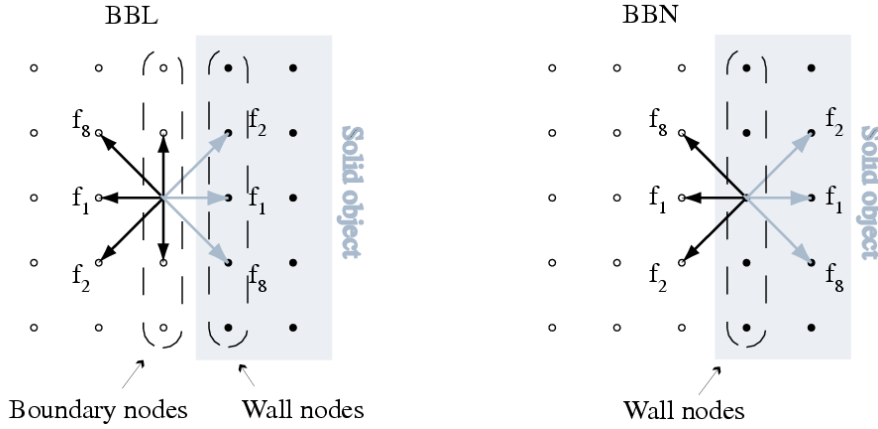


FIGURE 2.6 Bounce-back rules for stationary solid lattice nodes. Filled and open circles denote solid and fluid nodes, respectively, and the solid object is represented as a collection of solid nodes. We further distinguish wall nodes, which are those solid nodes that have fluid nodes in their neighbourhood. In BBL fluid nodes adjacent to the wall are called boundary nodes. Rest particles and links in boundary nodes pointing into fluid (black arrows) are classified as fluid links (FL) and correspondingly links pointing to the wall (grey arrows) are boundary links (BL). Populations before the collision with the wall (grey arrows) are "bounced back" to the direction where they came from (black arrows). In BBL particle densities travelling into wall at time t are flipped around during the same time step. In BBN densities are allowed to occupy wall nodes, where they are flipped around and travel back to the fluid node where they came from at the next time step $t + 1$.

For simple stationary flows (*e.g.* simple shear flows), the bounce-back condition (*i.e.* the location of the wall) is realised exactly in the middle of the link connecting the last fluid node and the solid node (wall node). For more complicated geometries the location of the wall is not well defined between the last fluid node and the wall node, and it depends on the relaxation parameter [33, 34].

The bounce-back rule is simple and computationally efficient. It can be modified so as to allow for moving boundaries [35],

$$f_i(\mathbf{r}, t+1) = f_{i'}(\mathbf{r}, t_+) + 2\rho_f \frac{w_i}{c_s^2} (\mathbf{u}_w \cdot \mathbf{c}_i) \quad (2.103)$$

at which the no-slip boundary condition is fulfilled. Here t_+ indicates the time immediately after the collision, i' denotes the bounce-back link, and \mathbf{u}_w is the velocity of the wall. The last term in Eq. (2.103) accounts for the momentum transfer between the fluid and the moving solid boundary.

Very thorough tests of the accuracy of the bounce-back rules together with more sophisticated boundary methods are reported in Ref. [34], and in the references therein. (See also the references in Ref. [23].)

In practice, fluid flow is often driven by pressure difference. This requires implementation of the pressure (density) or velocity boundary conditions in LBM [36, 37]. If the assumption of a constant pressure gradient across the system is valid, the pressure or the velocity boundary conditions can be replaced by a body force [38]. In the body force approach the effect of an external pressure gradient on the fluid is achieved by adding a fixed amount of momentum to the fluid particles at every time step.

In addition to inaccuracies due to boundary conditions (*e.g.* indefinite location of the no-slip condition), there are other sources of error in the LBM simulations such as finite-size effects and compressibility errors. (For a good overview of the error sources in LBM see Ref. [25]). In practice it may be difficult to determine exactly the total error. However, a practical error estimation can be made by doing simulations for several system sizes.

2.3.2 Suspension models

Lattice-Boltzmann models for suspensions have been developed *e.g.* by Ladd [34, 35, 39], Behrend [40], and Aidun [41]. In all these methods suspended particles are included in LBM by using their discrete images. All these methods give results that are in good agreement with each other and with results obtained by conventional simulation methods [40, 43, I, II]. The lattice points located inside a particle are assumed to belong to that particle. There are two different lattice points of this kind, the interior points and the boundary points. Each boundary point has at least one link c_i pointing to the fluid phase.

Interaction (the no-slip condition) between the surrounding fluid and a moving particle boundary are taken into account by applying the modified bounce-back condition Eq. (2.103) on the surface of the particle. Because of the no-slip condition, the fluid velocity on particle surface is $\mathbf{u}(\mathbf{r}) = \mathbf{U} + \boldsymbol{\Omega} \times (\mathbf{r} - \mathbf{R})$, where \mathbf{r} denotes a point on the surface, and \mathbf{U} , $\boldsymbol{\Omega}$, and \mathbf{R} denote particle velocity, angular velocity, and position, respectively.

The force and torque on the particle are obtained by integrating the total stress tensor \vec{M} over its surface. In practice this can be done by summing the effect of Eq. (2.103) at all boundary points. After this the trajectory of the particle, which moves in a continuous space, is determined by using Newtonian dynamics. This technique takes advantage of the fact that hydrodynamic interactions are time dependent and develop from purely local interactions at solid-fluid interfaces. Thus it is not necessary to consider the global solution, but one can update the motion of one particle at a time. The method scales linearly with the number of suspended particles and, therefore, allows far larger simulations than conventional methods.

The lattice-Boltzmann method can also be efficiently implemented for parallel processing [42]. Furthermore, electrostatic interactions, flow geometry, Peclet number (Brownian motion), shear rate and shear Reynolds number, as well as the size and shape of the suspended particles, can all be varied.

Ladd model

Differences between various suspension models arise mainly from their handling of the interior points. In the Ladd model the fluid fills also the suspended particles, and the solid-fluid interactions of Eq. (2.103) take place in the middle of the links (BBL) (*i.e.* each boundary point is located in the middle of a link). This is computationally very convenient, as there is now no need to create and destroy fluid when particles move. However, the interior fluid increases the effective mass and the effective moment of inertia of the suspended particles. This may affect particle dynamics in some cases [41], but as Ladd has shown [34], these effects are small as long as the contribution of the interior fluid to the inertia of the particle is taken into account. In addition, elastic frictionless collisions between suspended particles are highly dissipative due to the interior fluid, since there is a delay between the velocity change of the particle's shell and of the interior fluid. However, this has only a minor effect on suspension properties such as viscosity and shear stress [II]. Neutrally buoyant particles cannot be simulated by a method with interior fluid. The stability criterion for suspension models with interior fluid is given by [34]

$$\frac{\rho_s}{\rho_f} > 1 + \frac{10}{d}, \quad (2.104)$$

where ρ_s and ρ_f are the density of the particles and the fluid, respectively, and d is the diameter of the particles (in lattice units). Notice that for given ρ_s and ρ_f , this criterion gives the minimum size for particles that can be used to simulate realistic particle-fluid systems [34].

Aidun model

The method introduced by Aidun [41,43] is very similar to that of Ladd, but it does not include an interior fluid in the suspended particles. For this reason an algorithm is needed to create and destroy fluid when particles move. This may impose a perturbation to the surrounding fluid whenever a particle changes position. Also, some care must be taken with particle-particle and particle-wall collisions, as the lack of fluid between the touching solid walls may create an unphysically low pressure which must be eliminated. Because there is no interior fluid, there is also no limitation to the particle (mass) density in the simulations. The minimum particle size is limited only by the finite-size effects. (These effects, of course, concern all methods considered here).

Behrend model

A detailed analysis of various boundary rules were presented by Behrend in Ref. [40]. He also suggested a method, in which the particles are filled with fluid, but "a relaxed bounce-back" at the nodes (RBBN or modified BBN) is used instead of BBL. In this method the LBM collision phase is applied at every lattice node. The method is easy and efficient to implement because the bounce-back rule does not require any information about the locations of boundary links.

As mentioned before, in all LB-suspension models the centre point of a suspended particle moves in continuous space, but the boundary of the particle is discrete. Thus, when the particle moves, the number of the interior points, boundary points and the shape of the particle fluctuates. The effects of these fluctuations on the particle-particle hydrodynamical interactions are insignificant if the particles are large enough. Another possibility to minimise the effect of these fluctuations is to use the "continuous bounce-back rule" presented in Ref. [44] or the second order boundary conditions presented in Ref. [45]. These boundary rules allow the use of smaller particles, but they are more complicated to implement than BBL [34].

2.3.3 Multicomponent and multiphase models

A number of different approaches to simulate multicomponent and multiphase (liquid-gas) systems using the lattice-Boltzmann method have been presented during the last decade. We introduce here briefly the most frequently used models. (A good overview of the models considered here, excluding the colour model, can be found in Ref. [46].)

Colour model

The first lattice-Boltzmann model that was proposed for simulating immiscible binary fluids [47] was based on the colour lattice-gas model by Rothman and Keller [48]. This model was later extended to allow for variable density and viscosity by using the BGK lattice-Boltzmann approximation [49]. An extension to miscible fluids was introduced in Ref. [50]. A detailed description of the colour model can be found also in Ref. [24].

In the colour model, two distributions $f_i^{(r)}(\mathbf{r}, t)$ (red-particle distribution) and $f_i^{(b)}(\mathbf{r}, t)$ (blue-particle distribution) are used to represent two different fluids on link i . The distribution function for the entire fluid is defined as $f_i = f_i^{(r)} + f_i^{(b)}$. The lattice-Boltzmann equation Eq. (2.78) for $\alpha = r, b$ is now given by

$$f_i^{(\alpha)+}(\mathbf{r}, t) - f_i^{(\alpha)}(\mathbf{r}, t) = \Omega_i^{(\alpha)}(\mathbf{r}, t), \quad (2.105)$$

where $f^{(\alpha)+}$ is the post-collision distribution, and the collision operator is introduced in Eq. (2.81). The spatial separation and surface effects of the two fluids are achieved

by first computing the local colour gradient

$$\mathbf{F}(\mathbf{r}) = \sum_i \mathbf{c}_i (\rho_r(\mathbf{r} + \mathbf{c}_i) - \rho_b(\mathbf{r} + \mathbf{c}_i)), \quad (2.106)$$

and then perturbing the distribution function such that

$$f_i^{(\alpha)++}(\mathbf{r}, t) = f_i^{(\alpha)+}(\mathbf{r}, t) + \frac{A}{2} |\mathbf{F}| \left[\frac{(\mathbf{c}_i \cdot \mathbf{F})^2}{|\mathbf{F}|^2} - \frac{1}{D} \right]. \quad (2.107)$$

Here D is the dimension of the system, and A is a parameter which sets the magnitude of the surface tension. The next step is to redistribute the colour distribution functions in the lattice to ensure the separation of the two fluids. This can be done by choosing $f_i^{(r)++}$ and $f_i^{(b)++}$ such that

$$\sum_i (f_i^{(r)++} - f_i^{(b)++}) \mathbf{c}_i \cdot \mathbf{F} \quad (2.108)$$

is maximised without violating the conservation of colour, $\sum_i f_i^{(r)++} = \sum_i f_i^{(r)}$, and the conservation of total mass on each link, $f_i^{(r)++} + f_i^{(b)++} = f_i^{++}$. In other words, in this procedure the scalar product of the colour gradient and the colour flux is maximised. The final step of the method is the usual propagation step.

This procedure satisfies Laplace's law and (spontaneously) produces an interface between the two fluids [24, 47, 49]. The methods based on colour gradient have been used in several applications such as flow in porous media [51], droplet deformation [52], boiling water [53], and Rayleigh-Taylor instability [54]. However, a lack of consistent implementation of thermodynamics and an anisotropic surface tension that induces spurious currents near the interfaces, restrict the usefulness of the colour model in practical applications.

Local interaction model

This model is also known as the Shan-Chen model [55, 56, 57]. Here, in addition to the local collisions (Eq.(2.78)), neighbouring fluid particles exchange momentum at each node through an attractive short-range force given by

$$\mathbf{F}_G^\alpha(\mathbf{r}) = -\xi^\alpha \psi^\alpha(\mathbf{r}) \sum_{\alpha'}^S \sum_{i=1}^N G_i^{\alpha\alpha'} \psi^{\alpha'}(\mathbf{r} + \mathbf{c}_i) \mathbf{c}_i, \quad (2.109)$$

where α denotes different fluids, and ξ^α is the relaxation-time parameter for fluid α . (In other words, the force acting on the α 'th fluid can be found by summing over all fluids S and all neighbouring sites N .) A parameter $G^{\alpha\alpha'}$ controls the strength of the

surface tension between fluids α and α' . For the D_3Q_{19} model $G^{\alpha\alpha'}$ can be chosen as

$$G_i^{\alpha\alpha'} = \begin{cases} 2G^{\alpha\alpha'}, & \text{for } |\mathbf{c}_i| = 1, \\ G^{\alpha\alpha'}, & \text{for } |\mathbf{c}_i| = \sqrt{2}, \\ 0, & \text{for } |\mathbf{c}_i| = 0. \end{cases}$$

Notice that only the nearest-neighbour interactions are included in the model. In Eq. (2.109), $\psi^\alpha = 1 - \exp[-\rho^\alpha(\mathbf{r})]$ is an 'effective mass'. It has been shown [55, 56] that this form for the effective mass ψ leads to a non-ideal-gas equation of state. At large enough G two mixed fluids ($S = 2$) separate, and in the case of a single fluid ($S = 1$), transition to two separated phases occurs spontaneously.

Martys introduced adhesion forces between the fluid and solid phases by adding a force term [57]

$$\mathbf{F}_W^\alpha(\mathbf{r}) = -\xi^\alpha \psi^\alpha(\mathbf{r}) \sum_i W_i^\alpha s(\mathbf{r} + \mathbf{c}_i) \mathbf{c}_i, \quad (2.110)$$

where

$$W_i^\alpha = \begin{cases} 2W^\alpha, & \text{for } |\mathbf{c}_i| = 1, \\ W^\alpha, & \text{for } |\mathbf{c}_i| = \sqrt{2}, \\ 0, & \text{for } |\mathbf{c}_i| = 0, \end{cases}$$

where $s = 0, 1$ for liquid and solid, respectively. It is usually claimed that W is positive for a non-wetting and negative for a wetting liquid [57]. However, the wettability behaviour depends in addition on the cohesion strength G [58]. With these definitions, the surface tension force F_G and the adhesive force F_W change, at each time step, the momenta of fluid particles according to

$$\rho^\alpha(\mathbf{r}) \mathbf{u}'(\mathbf{r}) = \rho^\alpha(\mathbf{r}) \mathbf{u}(\mathbf{r}) + \mathbf{F}_G^\alpha(\mathbf{r}) + \mathbf{F}_W^\alpha(\mathbf{r}), \quad (2.111)$$

where \mathbf{u}' is the new fluid velocity to be used in Eq. (2.84).

Full details of the properties and benchmark studies of the Shan-Chen model are given in Refs. [55, 56, 57, 58, 59, 60, IV, V]. The surface tension model used in this approach also results in unphysical currents in the liquid-gas boundary layers because of lack of local momentum conservation. The surface tension is isotropic, and the total momentum is conserved [56]. Although the basic physical problems of the local interaction model are minor [60], more severe problems may arise from the fact that the width of the interface region is relatively large as compared with a typical length scale of the system [IV]. In addition, poor resolution near the solid-fluid boundary is a property of the model which must be taken into account [57, V]. In spite of its problems, the local interaction model can be used to simulate *e.g.* flows in porous media [57, 61], droplet collisions [62], droplet spreading [IV], capillary rise [V], bubble growth [63], and bubbly flows [64]. Both the colour and local interaction models are phenomenological models of interface dynamics, and are probably most suitable for isothermal multicomponent flows [23].

Free-energy model

The models mentioned above lack a clear relation to classical thermodynamics. The free energy model, developed at the University of Oxford [65, 66], introduces thermodynamics into the system in such a way that the evolution equation is the normal lattice-BGK equation Eq. (2.82), but a free-energy term is included through the equilibrium distribution function. The model satisfies the thermodynamic relations at equilibrium (*i.e.* the conservation of total energy) [67], but it has limitations in describing non-equilibrium dynamics. For example, the free-energy model does not obey Galilean invariance when density gradients are present, and its applications are thus limited. It has also been argued that the free-energy model presented in Refs. [65, 66] does not satisfy the Navier-Stokes equation [68]. Another problem is that the pressure tensor in the model is constructed without physical basis at the level of the Boltzmann equation [60]. However, the free-energy model has been quite successfully applied in studies of spinodal decomposition [69] and domain growth [70]. Other applications include droplet deformation [71] and gravitation waves [72].

Lattice-Boltzmann models for nonideal gases

In recent years, LBM multiphase models based on the Enskog equation have also been presented [60, 73, 74]. Enskog equation [60, 75] is a modified Boltzmann equation for dense gases which takes into account also intermolecular interactions, whereas in the models discussed above (the colour model, the local interaction model, and the free-energy model) the starting point is the original Boltzmann equation. The models based on the Enskog equation obey the correct thermodynamic equations (at least in equilibrium) and in this respect provide a significant improvement over the earlier models. A problem is, however, that the continuity equations of the models based on the Enskog equation contain density diffusion terms, and the momentum equations contain various unphysical terms [46].

Chapter 3

Viscosity of liquid-particle suspensions in Couette flow

In this chapter, we first present the results of several benchmarking studies for validation of the particular LB methods used in our suspension simulations. Then, we present several simulation results for the apparent viscosity, momentum transfer, and microscopic structure of non-Brownian suspensions. We also discuss reasons behind the shear-thickening behaviour of these suspensions for increasing shear rate. The Couette-flow geometry (shear flow) which is widely used here is relevant for many liquid-particle suspension applications, appearing *e.g.* in common viscometers.

3.1 Validation of the implemented methods

We used the Behrend method for 2D liquid-particle suspensions, and a parallelised Aidun method was implemented for 3D suspension simulations. The accuracy of these methods in 3D simulations has quite extensively been studied in Refs. [40] and [43].

In LB models, the hydrodynamic radius R_H of a suspended particle may differ from the input radius R . It is evident that in the 2D Behrend model the average R_H is systematically smaller than R , by about 0.4 (in lattice units) [I]. For example, for $\xi = 1$, when the input radius is $R = 10.0$ lattice units, the hydrodynamic radius is $R_H = 9.78$ lattice units for a fixed particle [I]. This is in contrast with the other two methods where hydrodynamic radius is closer to the input radius [39]. This difference is a consequence of the different realisations of the no-slip boundary condition. In the Behrend model, the no-slip boundary is close to the solid-wall points [40], whereas in the other two models it is at the midpoints of links.

Hydrodynamic radius (*i.e.* the location of the no-slip wall) is also a function of the LBM relaxation parameter [39] as we discussed above. We have tested this dependence in 2D suspension simulations. We noticed that the relative apparent

viscosity decreased by 9% (3%) when the relaxation parameter ξ changed from 1.0 to 0.55 for an area fraction of 30% (25%). Thus parameter ξ appears to have only a minor effect on the relative apparent viscosity in suspension simulations [I].

We have also studied hydrodynamic forces acting on a 2D disc with forced counterclockwise rotation close to a moving wall, and compared the results with those of a commercial finite-element solver (Fluent). The results (see Table 3 in Ref. [I]) show that agreement between the two methods is quite good. The biggest difference appears in the lift force, especially when the particle is very close to the moving wall. This is mainly due to the poor resolution in this case of the fluid between the surfaces of the wall and the particle.

When two particles approach each others they feel a strong repulsive force caused by the fluid being squeezed out of the gap. This kind of lubrication flows generate very high pressures in the gap [34]. We analysed the hydrodynamic lubrication forces between 2D cylinders in a central collision and in scattering with a non-zero impact parameter, and compared the simulated results (see Fig. 3.1) with the analytical results obtained for the same situation [76]. In both cases the relaxation-time parameter was $\xi = 1$.

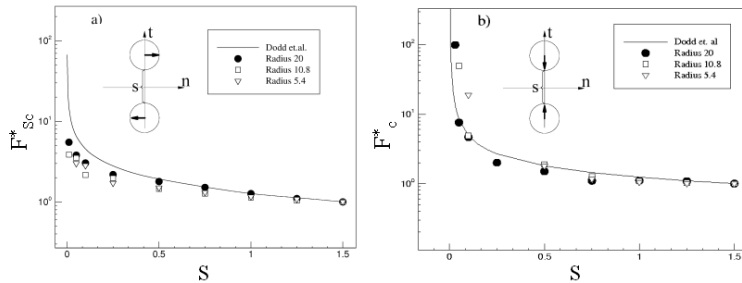


FIGURE 3.1 (a): Lubrication force on two particles scattering with a non-zero impact parameter as a function of the dimensionless impact parameter s . The full curve is an analytical result for the same situation [76]. The forces are scaled by the drag force imposed on a single particle by unperturbed fluid. (b): Lubrication force on two particles in central collision as a function of their dimensionless distance s . The full curve is an analytical results for the same situation [76]. The forces are scaled as in Fig. (3.1a).

In the central collision, the lubrication force is [76]

$$F_C = \mu_f \Delta U_n \frac{2^{3/2}}{s^{3/2}} \left[\frac{3}{4} J + \frac{3x_0}{4h_0} + \frac{s}{2} \left(\frac{207}{80} J + \frac{87}{80} \frac{x_0}{h_0} - \frac{3x_0}{8h_0^2} \right) + O(s^2) \right] \quad (3.1)$$

with $x_0 = \pi(s/2)^{-1/2}$, $h_0 = 1 + \frac{1}{2}x_0^2$ and $J = \sqrt{2} \tan^{-1}(x_0/\sqrt{2})$. The fluid viscosity is denoted by μ_f . In the scattering case the lubrication force is given by [76]

$$F_{Sc} = \mu_f \Delta U_t \frac{s^{1/2}}{\sqrt{2}} \left[3x_0 - \frac{J}{6} + \frac{4J}{s} + \frac{s}{2} \left(\frac{4x_0}{3} + \frac{x_0^3}{6} + \frac{7}{3} J \right) + O(s^2) \right]. \quad (3.2)$$

Here $s = (D_{12} - 2R)/R$ is the relative spacing between the two particles of radius

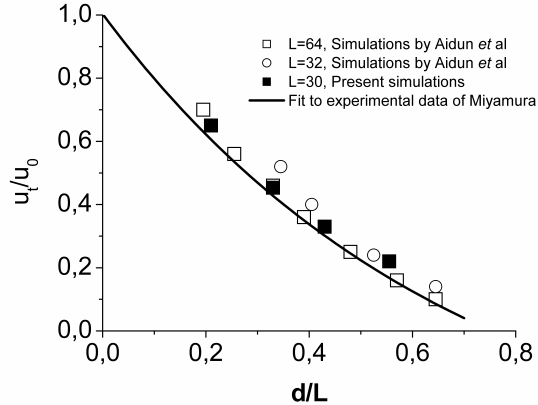


FIGURE 3.2 The terminal velocity of the particle u_t (divided by the unconfined terminal velocity) as a function of particle diameter d (divided by the wall width).

R with a centre-centre distance of D_{12} (here 1 and 2 denote the particles), $\Delta U_t = (\mathbf{U}_1 - \mathbf{U}_2) \cdot \mathbf{t}$ where \mathbf{U}_1 and \mathbf{U}_2 are the particle velocities and \mathbf{t} is a unit vector in the direction of motion of the particles, and $\Delta U_n = (\mathbf{U}_1 - \mathbf{U}_2) \cdot \mathbf{n}$ with \mathbf{n} a unit vector normal to the direction of the line connecting the particles at their shortest mutual distance. It is evident from Fig. 3.1 that the simulation results are in rather good agreement with the analytical solutions, especially in the case of central collision and for higher lattice resolutions [I]. If needed, the accuracy of the lubrication forces can be improved by calculating them directly from lubrication theory as has been done *e.g.* in Ref. [34].

To investigate the effect of lattice resolution we simulated 2D suspensions for three different resolutions, $R = 5.5, 11$ and 22 lattice units. (The full domain size for $R = 11$, *e.g.*, was $L_x \times L_y = 450 \times 130$ lattice units). For up to 30% area fraction, the relative apparent viscosity was almost independent of the resolution. For 40% area fraction, however, the difference in the relative apparent viscosity of the smallest and biggest resolution was already about 12% [I].

In order to test the correctness of the dynamics of a single particle, we carried out the 2D lateral migration test of Refs. [41, 77]. We found [II] that a particle initially placed near a wall migrated to the middle of the channel in good agreement with the results of Refs. [41, 77]. To validate our 3D parallel implementation of the Aidun method, we simulated the sedimentation of a single spherical particle in a square duct. In our test the particle was initially located with zero velocity in the middle line of a vertical square channel of width $L = 30$ lattice units. After this the particle started to fall along the middle line due to gravity, reaching finally its terminal velocity u_t . The unconfined terminal velocity u_0 was calculated from the Stokes equation. It is clear from Fig. (3.2) that our simulation results compare well with those of Ref. [41], and with the experimental data of Ref. [78].

Finally, in Fig. (3.3), we show our 2D (Behrend model) and 3D (Aidun model)

shear flow (Couette flow) simulation results for the relative apparent viscosity at a low Reynolds number as a function of the volume fraction (area fraction in 2D). Also the Krieger-Dougherty relation (see Eq. (2.76)) is shown for comparison. This relation agrees with the simulated data when the maximal packing fraction is $\phi_{\max} = 0.785$ and 0.68 for 2D and 3D, respectively. For these parameters the intrinsic viscosity $[\eta]$ in Eq. (2.76) has the value 2.4. We also show in Fig. (3.3) a number of previous experimental [79, 81] and numerical results [80] for Reynolds numbers smaller than unity. It is evident from this figure that our results agree with those of earlier studies. This agreement gives us confidence that the simulation model used captures the correct physics of the suspensions considered.

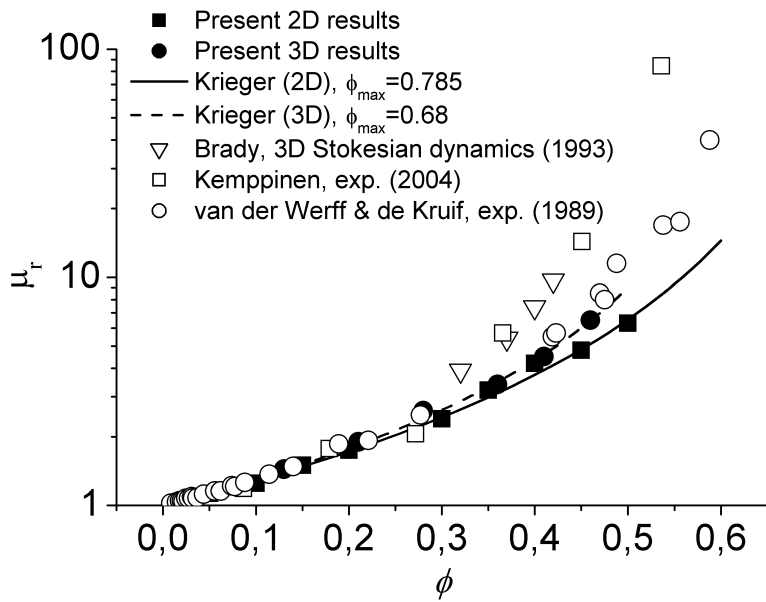


FIGURE 3.3 Comparison of the simulated relative apparent viscosity μ_r with previous experimental [79, 81] and numerical [80] results in 2D and 3D systems.

3.2 Some aspects of viscosity for non-Brownian liquid-particle suspensions

In all the following cases, we have simulated the dynamics of non-Brownian liquid-particle suspensions in a 2D Couette flow. The upper and lower walls of the flow channel move with a constant speed in opposite directions. Periodic boundary conditions are imposed between the inlet and outlet of the channel (see Fig. 3.4).

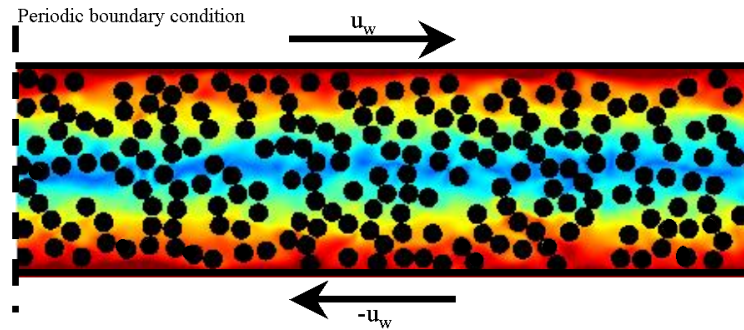


FIGURE 3.4 A snapshot of Couette flow of a liquid-particle suspension. The walls move in opposite directions creating a shear field. Fluid velocity is indicated by a colour scale so that red indicates high velocity. Periodic boundary conditions are imposed at the inlet and outlet of the channel (dashed lines).

3.2.1 Effect of particle shape

In addition to concentration (see Fig. 3.3), many other parameters - as we have already discussed in Section (2.2.2) - can affect the rheology of particulate suspensions. We studied the effect of particle shape on the relative apparent viscosity of the suspension with elliptical and star-like particles (a cross-shaped combination of two perpendicular ellipsoidal particles, with two different axis ratios a and major axes l : $a = 4.3, l = 17.2$ and $a = 3.0, l = 8.0$) [I]. Obviously, cf. Fig. (3.5), the relative apparent viscosity of the suspension is much higher for the star-shaped particles, with a given area fraction, than for the disc-shaped particles. This seems to be caused by the higher effective size of the star-shaped particles, and their much stronger tendency to form clusters. The viscosities of the suspensions of elliptical particles were found to be at most 10% larger than those of disc-shaped particles (not shown in Fig. (3.5)). The shape of the particles thus seems to have a significant effect on the relative viscosity of the suspension if the shape is very irregular.

3.2.2 Effect of shear rate

An important parameter in the rheology of suspensions is shear rate. We studied the shear-rate dependence of the viscosity of disc-particle [I, II, III] and star-particle

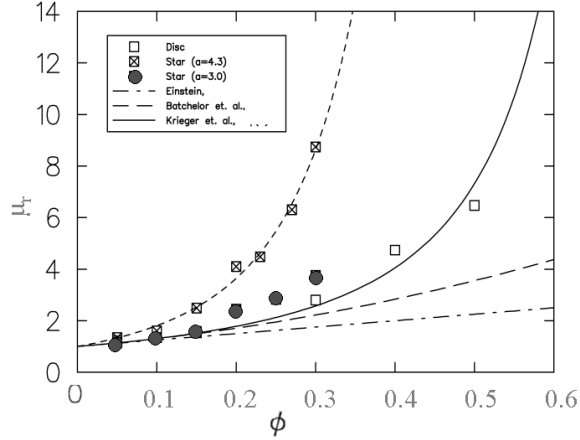


FIGURE 3.5 The simulated relative apparent viscosity η_r as a function of area fraction ϕ of suspended particles for different particle shapes. Dashed line is a best fit to the simulated points for star-like particles with $a = 4.3$, the other curves are the theoretical results of Einstein (see Eq. (2.74)), Batchelor (see Eq. (2.75)) and Krieger et al. (see Eq. (2.76)).

[I] suspensions for particle Reynolds numbers Re_γ varying from 0.0017 to 6, with $\xi = 0.55$. (The particle Reynolds number is defined as $Re_\gamma = d^2\dot{\gamma}/\nu_f$, where d is the particle diameter, $\dot{\gamma}$ the shear rate, and ν_f the kinematic viscosity of the fluid.) As is evident from Fig. (3.6), clear shear-thickening behaviour was found, *i.e.* the relative apparent viscosity increased with increasing shear rate. For dense systems and high shear rates this effect was particularly apparent. A strong dependence of the apparent viscosity on the shape of the particles could also be seen.

3.2.3 Cluster contribution to the viscosity of liquid-particle suspensions

At very low particle Reynolds numbers and in the absence of Brownian motion, the hydrodynamic forces acting on the particles are those of Stokes flow, and the particles move according to a linear (Newtonian) fluid-velocity profile until they encounter another particle. Because lubrication forces dominate particle-particle interactions, these 'collisions' are almost perfectly inelastic, which means that colliding particles will stay together for some time and form a cluster. These clusters will deform and rotate, merge into larger clusters and break up into smaller clusters or into individual particles. Large clusters are assumed to provide an efficient way for momentum transfer between channel walls, and to thereby increase the relative viscosity.

In order to analyse the dynamics of clusters, and their contribution to the relative viscosity, we first have to pay attention to their actual definition. A static cluster is easy to identify based on some neighbourhood criterion, *e.g.*, if two particles are separated by a distance of less than d , they belong to the same static cluster. In

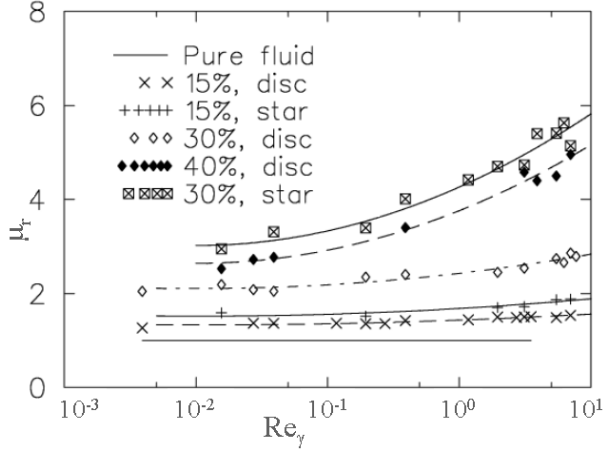


FIGURE 3.6 The relative apparent viscosity μ_r as a function of particle Reynolds number Re_γ for different particle shapes and solid area fraction. The lines are guides for the eye.

our case the distance d was chosen *e.g.* for disc-like particles as $d = 2.2 \times R$. This value for d was based on the radial pair- distribution function (PDF) such that it corresponded to the highest value of PDF. In the course of time clusters are however fused together and dissolved by some hydrodynamic fragmentation process. A problem is therefore to determine the identity of individual clusters in a suitable and consistent way, although there is no unique definition available. With our definition for a dynamic cluster we wanted to capture the relevant phenomena related to evolution of clusters. This means that we are interested in two different time scales: that of slow growth/shrinkage and that of fast fission/fusion of clusters. In the growth/shrinkage processes we wanted to follow the evolution of individual clusters, *i.e.*, to follow particular clusters that are growing/shrinking, whereas in the fission/fusion processes clusters may cease to exist. Figure (3.7) illustrates some relevant processes. The following definition for a dynamic cluster was thus chosen: We assume that a cluster identified at time t is the same as the one identified at time $t - \delta t$ if

$$\frac{N(t - \delta t) - N_{\text{old}}(t)}{N(t)} \leq K_1, \quad (3.3)$$

$$\frac{N_{\text{new}}(t)}{N(t)} \leq K_2, \quad (3.4)$$

provided that the cluster at t is connected to the one at $t - \delta t$ by an obvious trajectory. Here $N(t)$ is the number of particles in the cluster at time t , N_{old} is the number of 'old' particles (those that existed in the cluster already at the previous time step) at time t , and N_{new} is the number of 'new' particles in the cluster at time t . There is no unique definition for the parameters K_1 , K_2 and δt ; we choose here $K_1 = K_2 = 0.5$ and $\delta t = 200$ steps. We have analysed the evolution of each cluster in suspensions

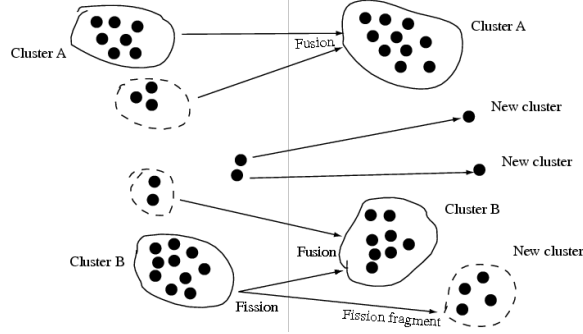


FIGURE 3.7 Illustration of relevant clustering processes.

by using these definitions. If the criteria of Eqs. (3.3) and (3.4) are not satisfied, the related cluster identified at time t is considered to disappear at time $t + \delta t$, and correspondingly new cluster/clusters are then born.

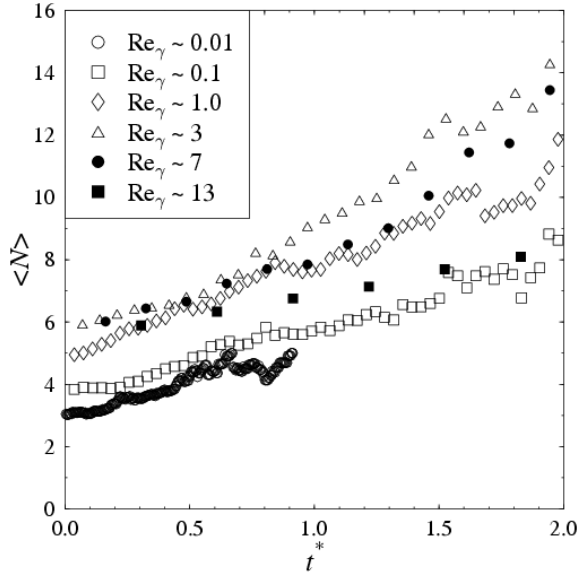


FIGURE 3.8 The average cluster size in 2D suspensions of disc-like particles ($\phi = 40\%$) as a function of the characteristic (dimensionless) life span t^* for different particle Reynolds numbers.

From the results of the dynamic cluster analysis described above, we found that the average decay time of the number of clusters is proportional to e^{-2t^*} , where $t^* = t\dot{\gamma}$ is a characteristic (dimensionless) time. During its time evolution, the average size of the clusters $\langle N \rangle$ varies as shown in Fig. (3.8), where $\langle N \rangle$ is shown as a function of the characteristic time t^* . The average size for each t^* is calculated over all clusters in the steady state that have life span t^* . As can be seen from figure (3.8), $\langle N \rangle$ increases with increasing particle Reynolds number in the regime $Re_\gamma \lesssim 1$, but remains almost constant for higher particle Reynolds numbers. It is evident that the average cluster size of disc-like particles does not correlate well with the relative

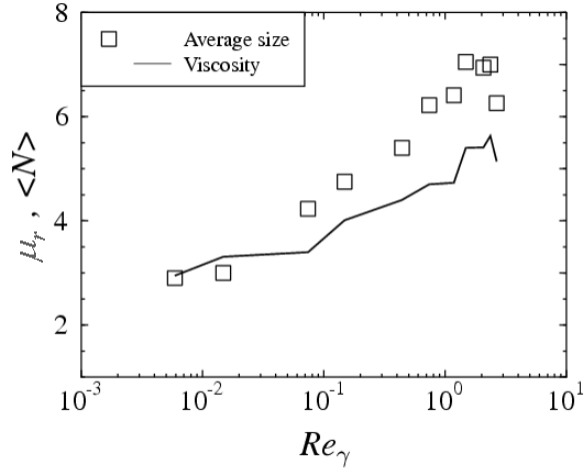


FIGURE 3.9 The average cluster size and relative apparent viscosity as a function of Re_γ for star-like particles with $\phi = 30\%$.

apparent viscosity when $Re_\gamma \gtrsim 1$. However, for star-like particles this kind of correlation exists as can be concluded from Fig. (3.9).

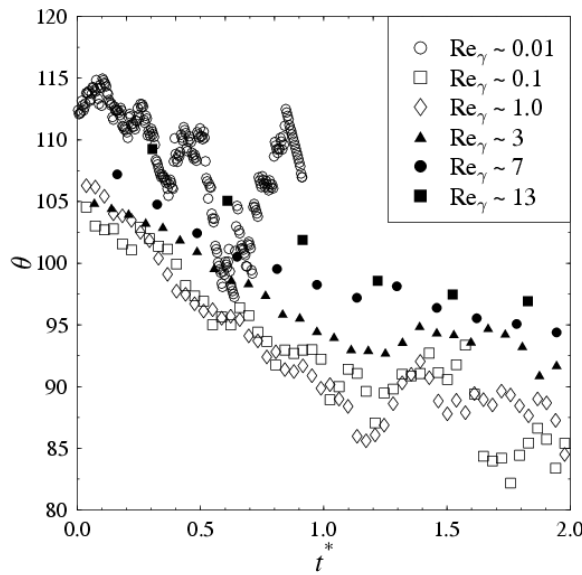


FIGURE 3.10 The average cluster orientation in the suspension of disc-like particles ($\phi = 40\%$) as a function of the characteristic (dimensionless) time t^* for different particle Reynolds numbers. Notice that, if the average angle is $\theta = 90^\circ$, cluster orientation is predominantly perpendicular to the flow direction.

In Fig (3.10) we show the average angle θ between the line connecting two fixed particles of the cluster and the direction of flow: $\theta = 180^\circ$ is upstream from the reference particles, $\theta = 0^\circ$ is downstream, and the angular dependences in the first and third quadrants, and in the second and fourth quadrants, are the same. As can be seen from the figure, the average orientation of the clusters is approximately per-

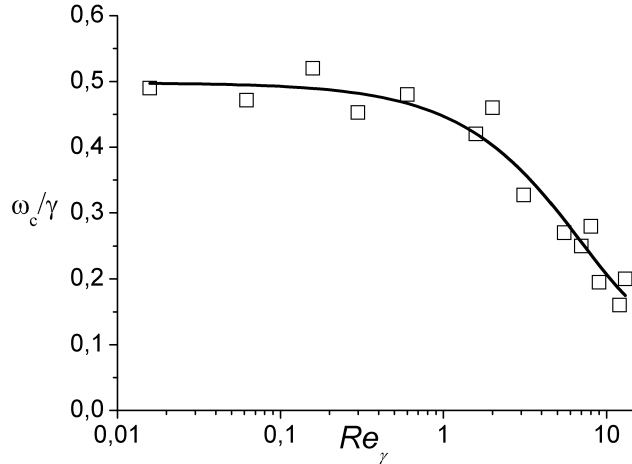


FIGURE 3.11 The dimensionless angular velocity of the clusters as a function of particle Reynolds number. The solid line is a fit by $0.4e^{-Re_\gamma/7}$ to the observed values.

perpendicular to the flow direction. In other words, clusters are born with the average angle $\theta \simeq 105 - 115^\circ$ and they die when $\theta \simeq 85 - 95^\circ$.

We also analysed the average angular velocity of the clusters. For low particle Reynolds numbers the average angular velocity is approximately $0.5\dot{\gamma}$ as expected, but it decreases with increasing shear rate when $Re_\gamma > 1$, as can be seen from Fig (3.11). Thus, there seems to be a correlation between decreasing average angular velocity and increasing relative viscosity.

Besides the average cluster size and the average orientation, we analysed the time evolution of the average cluster shape, which can be described by the second-rank tensor of the radius of gyration, $\tilde{\mathbf{S}}$. If the i 'th particle in a cluster of N particles is located at $\tilde{\mathbf{r}}_i = (\tilde{x}_i, \tilde{y}_i)$ with respect to the centre of mass, the tensor of the radius of gyration is given by

$$\tilde{\mathbf{S}} = \frac{1}{N} \begin{bmatrix} \sum_{i=1}^N \tilde{x}_i^2 & \sum_{i=1}^N \tilde{x}_i \tilde{y}_i \\ \sum_{i=1}^N \tilde{y}_i \tilde{x}_i & \sum_{i=1}^N \tilde{y}_i^2 \end{bmatrix} = \begin{bmatrix} S_{\tilde{x}^2} & S_{\tilde{x}\tilde{y}} \\ S_{\tilde{y}\tilde{x}} & S_{\tilde{y}^2} \end{bmatrix}, \quad (3.5)$$

where $S_{\tilde{x}^2}$ and $S_{\tilde{y}^2}$ denote the $\tilde{x}\tilde{x}$ and $\tilde{y}\tilde{y}$ components of the tensor. The trace of this tensor gives the scaled radius of gyration,

$$S_G^2 = Tr \tilde{\mathbf{S}} = S_{\tilde{x}^2} + S_{\tilde{y}^2}. \quad (3.6)$$

Therefore, $S_{\tilde{x}^2}$ and $S_{\tilde{y}^2}$ are also the \tilde{x} and \tilde{y} components of the scaled radius of gyration. If the cluster shape is described as an ellipse, the two squared principal axes

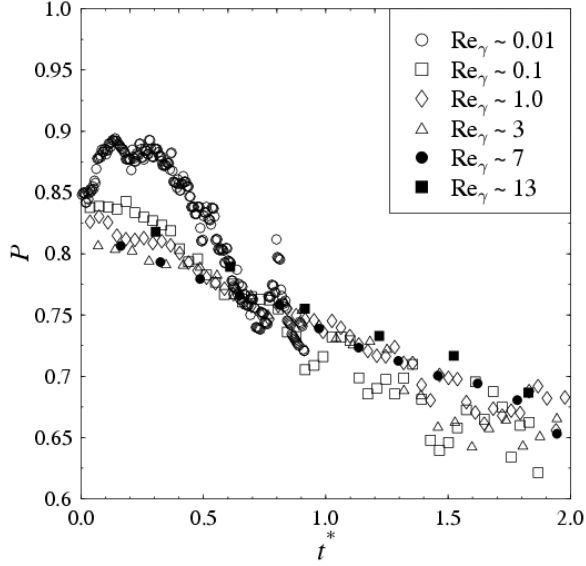


FIGURE 3.12 The average shape factor of the suspension of disc-like particles ($\phi = 40\%$) as a function of the characteristic (dimensionless) time t^* for different particle Reynolds numbers. For rod-like cluster $P = 1$, and $P = 0$ for spherical clusters.

λ_{\max} and λ_{\min} can be expressed in the form

$$\begin{aligned}\lambda_{\max} &= \frac{1}{2}S_G^2 + \lambda, \\ \lambda_{\min} &= \frac{1}{2}S_G^2 - \lambda,\end{aligned}\quad (3.7)$$

with

$$\lambda = \sqrt{\frac{1}{4}(S_{\tilde{x}^2} - S_{\tilde{y}^2})^2 + S_{\tilde{x}\tilde{y}}^2}. \quad (3.8)$$

The degree of anisotropy can be described by a shape parameter

$$P = \frac{2\lambda_{\max}}{S_G^2} - 1, \quad (3.9)$$

with $P \in [0, 1]$. $P = 0$ and $P = 1$ correspond to a sphere and a rod, respectively.

The time evolution of the average shape parameter of the clusters is shown in Fig.(3.12). For all particle Reynolds numbers, clusters are clearly rod-like rather than spherical. However, clusters seem to compress slightly during rotation.

We can conclude from the dynamic cluster analysis that particles form rod-like clusters on the upstream side ($\theta > \frac{1}{2}\pi$), they rotate and are compressed, and are finally destroyed by shear forces on the downstream side ($\theta < \frac{1}{2}\pi$). The rotation and compression of the clusters indicate their ability to transmit momentum (or stress) perpendicular to the flow direction [84]. This, together with the bigger average cluster size, could explain the higher relative apparent viscosity of the star-particle suspensions in comparison with the disc-particle suspensions.

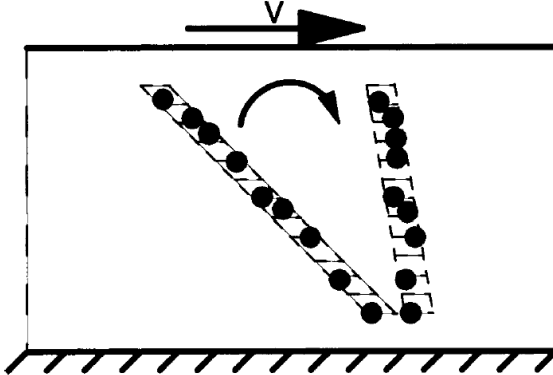


FIGURE 3.13 Schematic presentation of the KCM model.

Based on the results of this dynamic cluster analysis we constructed a schematic model called the Kinetic Clustering Model (KCM) [III]. The idea of KCM is the following: Consider the part of a suspension located within a long and narrow tubular volume element at a small angle across the shear cell (flow channel) such that flow velocity at the trailing end is higher than that at the leading end of the element (see Fig. (3.13)). As this imaginary tube rotates in the shear velocity field, it will become broader and shorter. Initially, when the tube is very long and narrow, the particles that have their centres of mass within the tube are located far from each other in an uncorrelated fashion. The density of the centres of mass then obeys a Poisson distribution. As the element rotates, particles will come closer to each other and begin to collide. According to KCM, the cluster-size distribution $n(m)$ in a low Reynolds number Couette flow (in the absence of Brownian motion) is found to be [III]

$$n(m) \propto m^{-1.5} \exp\left(-\frac{m}{m_0}\right). \quad (3.10)$$

Here m is the cluster size (the number of particles in the cluster) and

$$m_0 = m_0^{KCM}(\lambda) \equiv 1/(\lambda - \log(\lambda) - 1), \quad (3.11)$$

where $\lambda = \phi/\phi_c$. The distribution $n(m)$ is scale invariant for $m \ll m_0$, and it decreases rapidly for $m > m_0$. The cutoff cluster size m_0 diverges when the solid volume fraction ϕ reaches its critical value ϕ_c , which indicates that infinitely large clusters (in the thermodynamic limit) appear in the system in this limit. This divergence represents a jamming limit at which viscosity is expected to diverge [82]. Since m_0 is the only variable related to clustering, we would expect the relative viscosity in the Stokes-flow regime to be of the form

$$\mu_r = 1 + f(m_0), \quad (3.12)$$

in which 1 relates to the viscosity of the pure fluid, and f is an unknown function

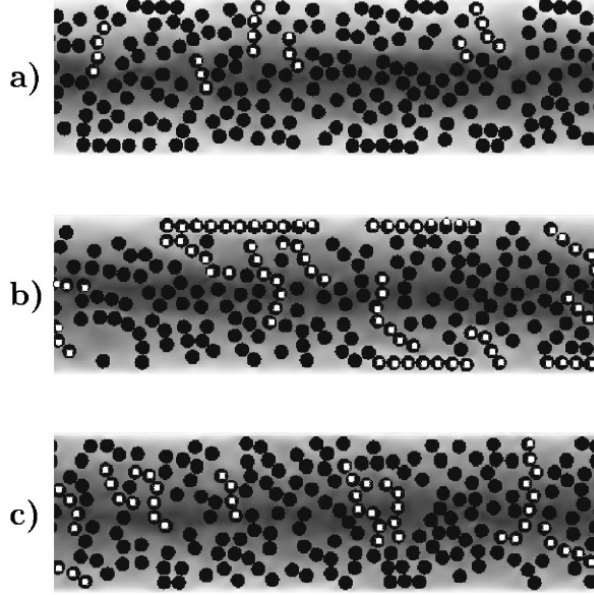


FIGURE 3.14 Snapshots of liquid-particle suspensions for $Re_\gamma = 0.1$ (a), $Re_\gamma = 1$ (b), and $Re_\gamma = 10$ (c). A few clusters are indicated. The walls 130 lattice units apart move in opposite directions creating a shear field. Fluid velocity is indicated by a grey scale so that white indicates high velocity.

that describes the part of the viscosity which originates from the clustered particles.

In order to test Eq. (3.10), and to extract function f , we performed LB simulations of liquid-particle suspension in two-dimensional shear flow [III]. Figure (3.14) shows snapshots of suspensions for particle Reynolds numbers $Re_\gamma = 0.1, 1$, and 10 . Some typical particle aggregates are indicated in the figure. Two types of aggregates with quite distinct characteristics indeed appear in the two-dimensional flow. Near the moving walls, horizontal ‘layers’ of particles can be found. (In accordance with the common view discussed in Section 2.2.2 and in Ref. [III]). These layers appear at relatively low Reynolds numbers ($Re_\gamma \lesssim 1$) but disappear when $Re_\gamma \gtrsim 1$. It is interesting that this layering did not appear in Stokes flow. (In these simulations flow was forced to be linear by omitting the nonlinear terms from Eq. (2.84).) Instead, suspended particles began to concentrate in the middle of the channel for $Re_\gamma \gtrsim 1$. The dynamics of particle layers is subject to future work, here we just make a few qualitative observations. In the interior of the flow channel, chain-like clusters form and rotate under the shear flow much in accordance with the generic clustering model discussed above and in Ref. [III].

In the entire region covered by the present simulations, the size distribution of the rotating clusters is indeed given by Eq. (3.10) as predicted by the kinetic clustering model (see Fig. 3.15(a)). Thus, m_0 is the only parameter indicative of cluster size. In general it may, however, depend on both the volume fraction of particles and on the particle Reynolds number. Based on our numerical simulations [III], three distinct flow regimes can be found concerning the characteristics of the flow: a viscous

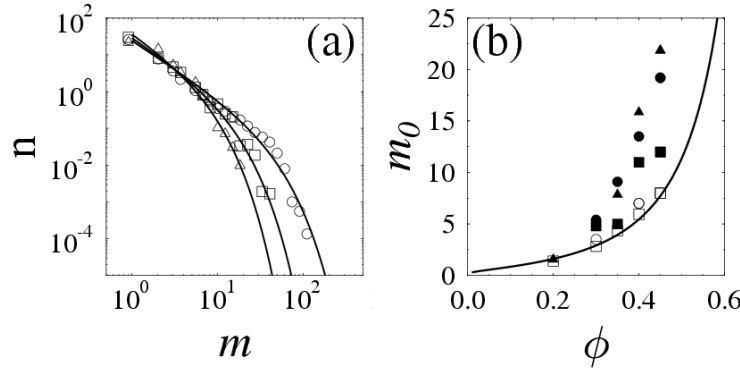


FIGURE 3.15 (a) Cluster-size distributions for $\phi = 0.4$: $Re_\gamma = 0.01(\triangle)$, $Re_\gamma = 0.1(\square)$, $Re_\gamma = 1.0(\circ)$. The solid lines indicate the distributions predicted by KCM. (b) m_0 as a function of ϕ for $Re_\gamma = 0.06(\square)$, $0.3(\blacksquare)$, $0.8(\bullet)$, $1.4(\blacktriangle)$; channel width is $h = 130$. For $Re_\gamma = 0.06$ another channel width was also used: $h = 260(\circ)$. The solid line is the theoretical relation Eq. (3.11).

regime for $Re_\gamma \lesssim 0.1$, a transition regime for $Re_\gamma \sim 1$ and an inertial regime for $Re_\gamma \gtrsim 10$.

In the viscous regime there are no visible wall layers and the average size of the rotating clusters is small (see e.g. Fig. 3.14(a)). A comparison between Eq. (3.11) and simulation results reveals a close to perfect match within this regime (see Fig. 3.15(b)). For larger Reynolds numbers m_0 increases considerably. In the viscous regime the average velocity profile across the channel has only small fluctuations away from a Newtonian (straight) profile, which is demonstrated by Fig. 3.16(a). This region is thus the realm of laminar Stokes flow. We would consequently expect the effective viscosity to have little (if any) Reynolds number dependence. This is confirmed in Fig. 3.16(b). We can then proceed to extract the function f of Eq. (3.12). This can be done by plotting $\mu_r - 1$ as a function of m_0 . The result is shown in Fig. 3.17. For the lowest Reynolds numbers a linear function $f(m_0) \approx 0.5m_0$ gives a reasonable fit to the simulation data. It is also worth noticing that when this form of f is inserted in Eq. (3.12), the semi-empirical Krieger formula is regained for λ close to unity. For comparison the Krieger formula $(1 - \lambda(m_0))^{-2}$ is also displayed in Fig. (3.17). In the viscous regime we thus have

$$\begin{aligned} m_0 &= m_0^{KCM}(\lambda) \\ \mu_r &= \mu_r(m_0) \approx 1 + 0.5m_0 \approx (1 - \lambda(m_0))^{-2}, \end{aligned} \quad (3.13)$$

which means that the effective viscosity depends only on m_0 , and this is given by the KCM model. With m_0 determined, the effective viscosity can be extracted approximately using either Krieger formula or $f = 0.5m_0$.

In the transition regime wall layers develop and reach their maximum average size (actually, the maximum size appears before $Re_\gamma = 1$). Also the size of the rotat-

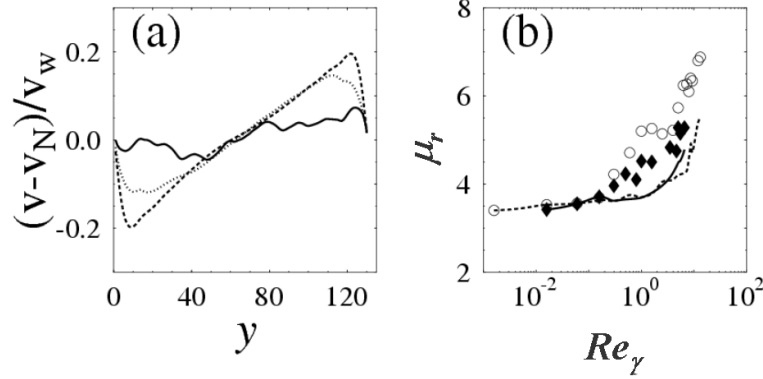


FIGURE 3.16 (a) Difference of the simulated (v) and Newtonian (v_N) velocity profile, normalized by the wall velocity (v_w), as a function of distance from the lower wall, for $Re_\gamma = 0.1$ (solid line), $Re_\gamma = 1.0$ (dotted line), and $Re_\gamma = 10.0$ (broken line). (b) Apparent and intrinsic viscosities as functions of Re_γ for $h = 130$ (broken line, \circ), and $h = 260$ (solid line, \blacklozenge), respectively.

ing clusters (i.e. m_0) grows considerably. Both these effects are visible in Fig. 3.14(b). However, m_0 is no longer given by Eq. (3.11) as can be seen from Fig. 3.15(b). The effective viscosity grows in this regime but not in proportion to the increase in m_0 . In this regime

$$\begin{aligned} m_0 &= m_0(\lambda, Re_\gamma) > m_0^{KCM}(\lambda) \\ \mu_r &= \mu_r(m_0, Re_\gamma) < 1 + 0.5m_0. \end{aligned} \quad (3.14)$$

So KCM fails, except for the cluster-size distribution. The velocity profile deviates from the Newtonian profile and an S-shaped profile with a higher shear close to the walls is developed (see Fig. 3.16(a)). Consequently, two different definitions of viscosity are possible: intrinsic viscosity, which is a bulk property determined using the shear rate in the middle of the channel, and apparent viscosity determined using the average shear rate (measurable but affected by the flow profile, *i.e.*, by boundary layers). The two viscosities are displayed in Fig. 3.16(b) for a few values of Re_γ . For increasing distance between the moving walls, the velocity profile becomes closer and closer to the Newtonian (linear) profile (also the two viscosities are more and more equal). This indicates that the influence of boundary layers is restricted to finite system sizes.

Above $Re_p \sim 10$ flow instabilities arise signifying an incipient inertial regime. In this case particle layers near the walls largely disappear. The typical cluster size inside the flow region also starts to decrease due to stronger velocity fluctuations. This is seen as a slight decrease of m_0 when compared to the transition regime (Fig. 3.17(b)). The S shape of the velocity profile becomes more pronounced (Fig. 3.16(a)), and μ_r increases rapidly with increasing Re_γ (Fig. 3.16(b)). We can conclude that an increasing cluster size does not alone explain (directly) the increasing viscosity

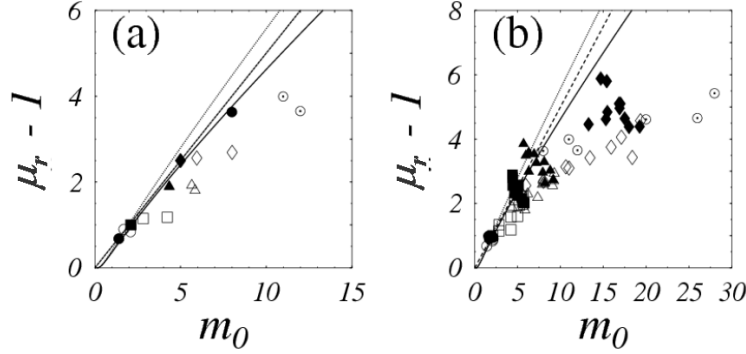


FIGURE 3.17 (a) $\mu_r - 1$ as a function of m_0 for $\text{Re}_\gamma \leq 1$ and $\phi = 0.2(\circ), 0.3(\square), 0.35(\triangle), 0.4(\diamond), 0.45(\odot)$. The filled symbols indicate $\text{Re}_\gamma = 0.06$. (b) $\text{Re}_\gamma \leq 13.0$. Filled symbols correspond to the inertial regime. The solid line and the dotted line indicate the results of Krieger formula with exponents of -1.8 and -2.0 , respectively. The broken line is $1 + 0.5m_0$.

at higher particle Reynolds numbers. (This was already concluded earlier from the dynamic cluster analysis).

3.2.4 Momentum transfer

Viscosity is a transport coefficient which measures the efficiency of momentum transfer across the system under consideration. On the other hand, for incompressible Newtonian fluids under shear flow, we can calculate the viscosity $\mu = -\tau / (\frac{dv_x(z)}{dz})$ which provides all material information we need to specify the constitutive equation (see, e.g., Eq. (2.60)). For non-Newtonian fluids, like liquid-particle suspensions, this process is more complicated because of bigger number of momentum transfer mechanisms. In order to specify the constitutive equation of a liquid-particle suspension, we need to understand the underlying mesoscopic mechanisms that contribute to the viscosity (especially in the inertial regime). Therefore, we determined the stresses and momentum fluxes in different phases, including the viscous stress in the fluid phase, the structural stress inside the particles, and the (convective) inertial fluxes that arise from the pseudo-turbulent fluctuations of the both solid and fluid phases [II].

The total momentum flux \mathbf{F} through any surface S in the suspension is given by

$$\mathbf{F} = \int_S \vec{\Pi} \cdot d\mathbf{S}, \quad (3.15)$$

where $\vec{\Pi}$ is the total momentum tensor. In the present case it can be written in the form

$$\vec{\Pi} = \vec{\mathbf{C}}_f + \vec{\mathbf{C}}_s + \vec{\mathbf{M}}_f + \vec{\Sigma}_s, \quad (3.16)$$

where $\vec{\mathbf{C}}_f$ and $\vec{\mathbf{C}}_s$ are the convective momentum tensors, and $\vec{\mathbf{M}}_f$ and $\vec{\Sigma}_s$ are the

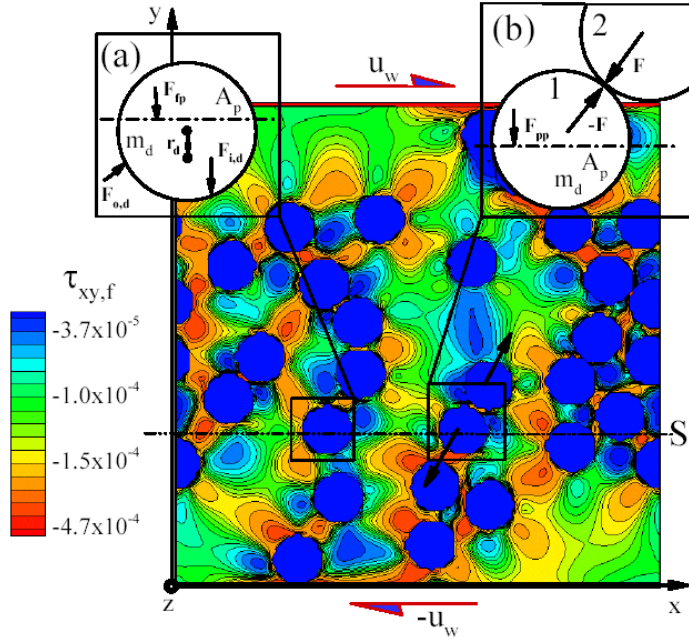


FIGURE 3.18 A snapshot of a two-dimensional Couette-flow of a liquid-particle suspension as solved by the LB method. Colour coding indicates viscous shear stress in the fluid phase. The two insets show the forces used in determining the internal particle stress.

internal stress tensors for the fluid and the solid phase, respectively [II]. A schematic illustration of the simulation setup together with a snapshot of an actual solution for the Couette flow of the 2D suspension is shown in Fig. 3.18. Here the surface $S = S(y)$ is a plane perpendicular to the y axis. The total shear stress acting on this plane is

$$\tau_T = \sigma_f + \sigma_s + \tau_f + \tau_s, \quad (3.17)$$

where stresses σ_f and σ_s contain the stresses due to pseudo-turbulent motion of the two phases, τ_f contains the viscous stress of the fluid phase and τ_s contains the internal stress of the particles [II]. Stresses σ_f , τ_f and σ_s can all be directly determined at each lattice point using Eqs. (2.89), (2.90) and (2.91). The stress τ_s can be determined from the collisions of the particles and from the hydrodynamic forces acting on their surfaces [II]. In Table 3.1 we show the relative contributions of the four different momentum transfer mechanisms for two solid volume fractions $\langle \phi \rangle$. The convective (pseudo-turbulent) stresses are very small when compared to the other stress terms, and will not be considered in the following. In Fig. 3.19 we show the ratio of the shear stress carried by the fluid, τ_f , and the shear stress carried by the particles, τ_s , to the total shear stress as a function of the particle Reynolds number Re_γ . Figure 3.20 shows the same ratio as a function of the average solid volume fraction at a fixed particle Reynolds number $Re_\gamma \approx 3$. As evidenced by Fig. 3.20, the contribution of the solid phase to the total shear stress strongly increases with

$\langle \phi_s \rangle$	σ_f / τ_T	σ_s / τ_T	τ_f / τ_T	τ_s / τ_T
12%	0.013	0.057	73.98	26.03
52%	0.083	0.196	11.30	88.33

TABLE 3.1 Relative contributions of the different momentum-transfer mechanisms to the total shear stress τ_T for two values of the average solid volume fraction. Stresses σ_f and σ_s are the pseudo-turbulent stresses of the fluid and solid phases, respectively, τ_f is the viscous stress of the fluid phase, and τ_s is the solid stress (internal shear stress in the suspended particles).

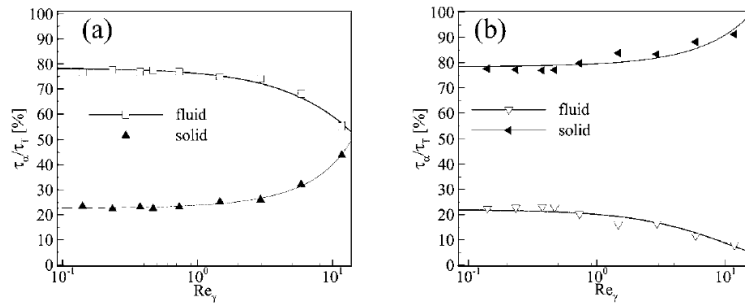


FIGURE 3.19 The ratio of viscous stress τ_f and solid stress τ_s to the total shear stress τ_T as a functions of the particle Reynolds number Re_γ , for a suspension with $\langle \phi_s \rangle = 12\%$ (a), and for a suspension with $\langle \phi_s \rangle = 52\%$ (b).

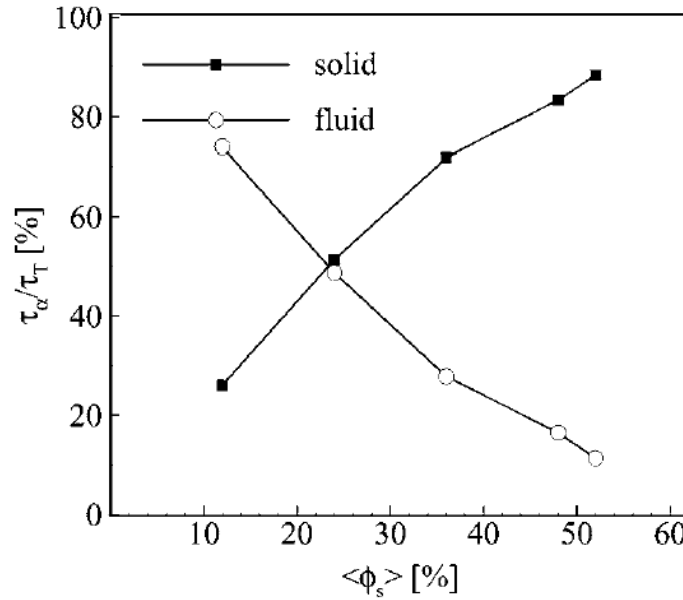


FIGURE 3.20 The ratio of viscous stress τ_f and solid stress τ_s to the total shear stress τ_T as a function of the average solid volume fraction $\langle \phi_s \rangle$ for $Re_\gamma \approx 3$.

increasing solid volume fraction. Less obvious is the behaviour of the relative contributions of the two phases as functions of the shear rate. As shown in Fig. 3.19, the

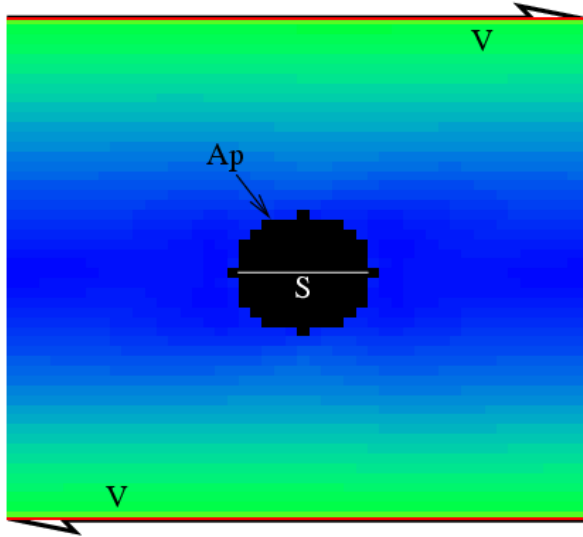


FIGURE 3.21 A fixed, freely rotating particle on the neutral line of a shear velocity field.

relative shear stress of the solid phase is nearly independent of Re_γ at low particle Reynolds numbers, but begins to increase with Re_γ increasing beyond unity. Comparing, *e.g.*, with Fig. 3.16(b), one is tempted to conjecture that this phenomenon is related to shear thickening, *i.e.*, the observed shear thickening is related to enhanced relative solid phase stress for increasing shear rates [II].

3.2.5 Solid phase stress

The solid-phase stress τ_s is a sum of pressure and viscous stresses τ_f acting on the particle surfaces. In order to investigate the origin of the solid-phase stress as a function of Re_γ , we implemented the simulation setup of Fig. 3.21 with only one fixed, freely rotating particle on the neutral line of the shear field. Particle radius was 6 lattice units and the side length of the square simulation domain was 50 lattice units. Periodic boundary conditions were imposed at the inlet and outlet of the channel. (We also repeated the same simulations in 3D. The results of the latter simulations were qualitatively similar to the results reported here [84].) Next we determined the pressure stress (force) and the viscous stress (force) acting on the surface A_p of the upper half of the particle. Because the particle was fixed and its angular velocity was constant (*i.e.*, the simulation had reached a steady state), the mean force acting on plane S is

$$\mathbf{F}_s = \int_{A_p} \vec{\mathbf{M}}_f \cdot d\mathbf{S} = \int_{A_p} p d\mathbf{S} - \int_{A_p} \vec{\tau}_f \cdot d\mathbf{S}. \quad (3.18)$$

We performed simulations using the both nonlinear (Navier-Stokes equation) and linear (Stokes equation) version of the LB equation (by removing the nonlinear terms from Eq. (2.84)). For the Stokes flow the total shear force acting on plane S inside the

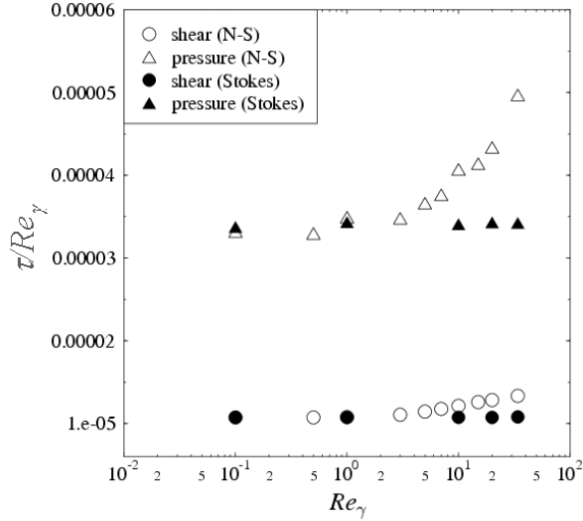


FIGURE 3.22 Scaled pressure and the viscous components of the total shear force as functions of Re_γ .

particle was found to increase linearly with increasing shear rate, and the apparent viscosity was constant in the entire regime covered by the simulations. For the Navier-Stokes flow the total shear force inside the particle was a linear function of Re_γ when Re_γ was small, but increased faster for $Re_\gamma > 1.0$. (See Fig. 3.22, where the scaled pressure and the viscous components of the total shear force are separately plotted as functions of Re_γ .) The pressure component of the total shear force now dominates. So, even in this very simple and very dilute ‘suspension’ the apparent viscosity begins to increase for $Re_\gamma > 1.0$ (see Fig. 3.23). Another interesting result

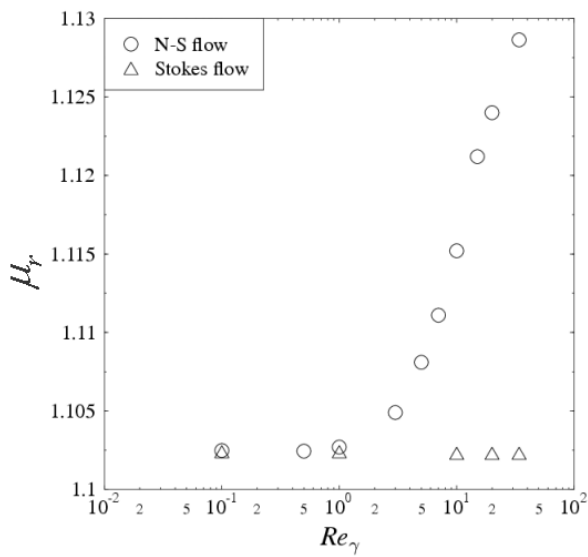


FIGURE 3.23 Apparent viscosity as a function of Re_γ .

was that the relative angular velocity of the particle slowed down for $Re_\gamma > 1$. This did not happen in the Stokes flow (see Fig. 3.24). At the same time when the relative angular velocity of the particle decreased, we observed increasing reverse flow on both sides of the particle (the relative volume flow in the gaps between the moving walls and the particle surface decreased). As mentioned before, the angular velocity

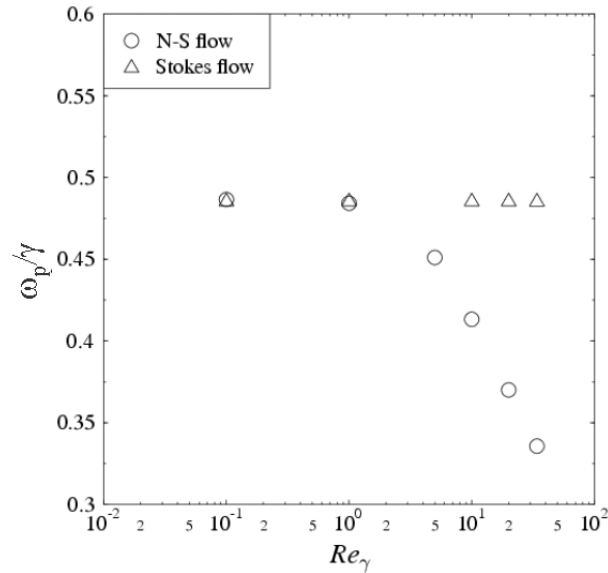


FIGURE 3.24 The angular velocity of the particle as a function of Re_γ .

of the clusters behaved similarly. We can conclude that the relative shear stress inside the particles increases with increasing Reynolds number implying that inertial effects begin to affect suspension rheology for $Re_\gamma \gtrsim 1$.

Chapter 4

Liquid droplet on a porous surface

In this chapter, we first present the results of several benchmarking studies for validation of the particular LB method used in our droplet-spreading simulations. Then we present some preliminary results from our study of droplets on the surface of a porous medium including their impact, spreading and penetration.

4.1 Validation of the implemented method

We have used here a three-dimensional version of the parallelised local interaction model (Shan-Chen model). We have performed several tests to verify that our implementation of the simulation method produces physically correct behaviour [IV]. In Fig. 4.1 we demonstrate the validity in this case of Laplace's law which states that, for a free droplet of radius r_0 , the pressure difference Δp across the droplet surface is in equilibrium related to surface tension γ and droplet-surface curvature $\kappa \equiv 1/r_0$ such that $\Delta p = 2\gamma\kappa$. Surface tension can thus be evaluated from the slope of the Δp curve as a function of κ .

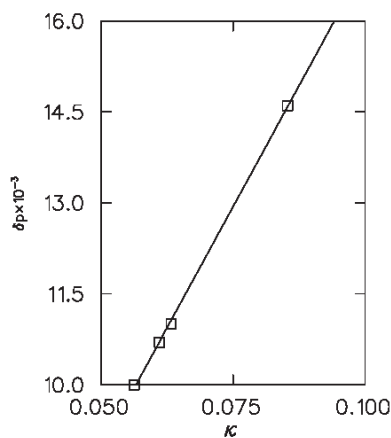


FIGURE 4.1 The relation of droplet curvature κ and the pressure difference Δp .

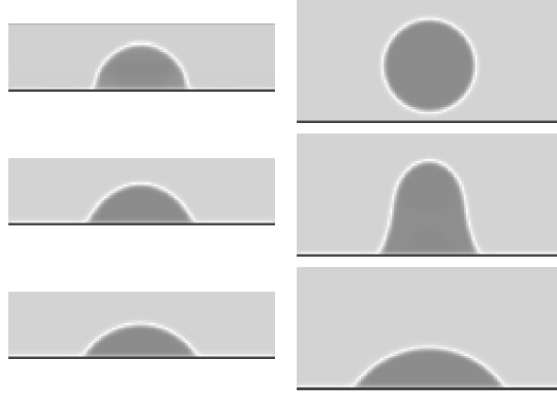


FIGURE 4.2 Snapshots of droplet spreading on a smooth surface for two initial conditions. The topmost snapshots show the initial configuration and the lowermost snapshots show the steady-state or final configurations.

We have simulated the spreading process of a droplet on a flat surface [IV]. Some snapshots of the spreading process are shown in Fig. 4.2. For a relatively flat initial droplet shape (as in the case of Fig. 4.2 (left)) we observed that the time evolution of the droplet radius R , which was measured along the plane of the surface, is consistent with the well-known Tanner's law $R \sim t^q$ with $q = 1/10$ [83].

In order to test the use of LBM to model imbibition of a fluid in a porous medium, we have simulated the capillary rise phenomenon [V]. In Fig. 4.3 we present the main result of our capillary simulations at zero gravity. Here the height of the column is shown as a function of time for four values of tube radius r with $W = -0.1$ (see Eq. (2.110)). For increasing tube radius the column rises faster, as expected. The solid lines in Fig. 4.3 show the corresponding numerical solutions of the equation

$$\rho_f \left[\frac{1}{2} \left(\frac{dh}{dt} \right)^2 + h \frac{d^2h}{dt^2} \right] = \frac{2\gamma \cos \theta_d}{r} - \frac{8\mu(h + h_+)}{r^2} \frac{dh}{dt} - \rho_f gh, \quad (4.1)$$

where h is the height of the rising column measured from the level of the liquid surface outside the tube, h_+ is the length of the part of the capillary tube immersed in the liquid, and r is the radius of the tube. Fluid density, viscosity, surface tension and dynamic contact angle are denoted by ρ_f , μ , γ , and θ_d , respectively. By neglecting the inertial and the inlet pressure from Eq. (4.1), the classical Washburn equation [85] for capillary rise is obtained:

$$8\mu(h + h_+) \frac{dh}{dt} = 2r\gamma \cos \theta - r^2 \rho_f gh. \quad (4.2)$$

Due to the rough discretization and the density variation (see Fig. (4.4) below) especially for small r , it is difficult to accurately measure θ_d directly from the density field. For an indirect determination of θ_d , we first apply the one-dimensional

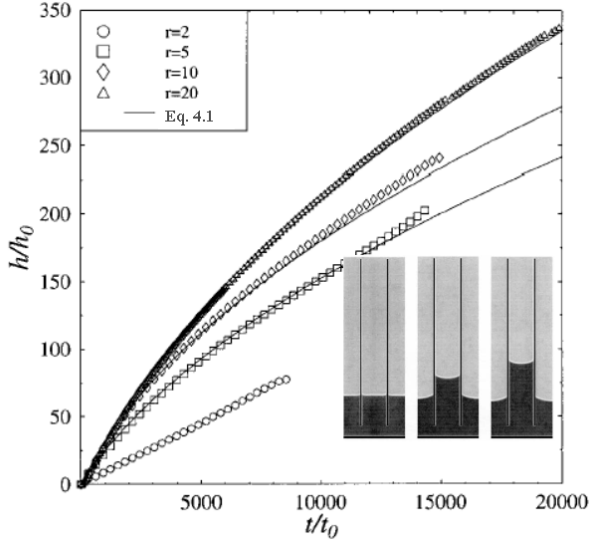


FIGURE 4.3 The height of the fluid column as a function of time for $r = 2, 5, 10$ and 20 lattice units. Numerical solutions of Eq. (4.1) are also shown. The insets show snapshots of capillary rise.

Reynolds transport theorem for a control volume to estimate the rate of change of the momentum of the system. The upper control surface moves with the meniscus of the liquid column (no outflow from the control volume) and the lower control surface is fixed at the lower end of the tube. Then the rate of change of the total momentum inside the control volume is

$$\frac{d}{dt}(mv)_{syst} = \frac{d}{dt} \left[\int_{CV} \mathbf{v} \rho dV \right] + \int_{CS} \mathbf{v} \rho (\mathbf{v} \cdot \mathbf{n}) dA, \quad (4.3)$$

where $m = m(t)$ is the total mass of the fluid inside the control volume, \mathbf{v} is the fluid velocity, and CV and CS denote the volume and surface area of the control volume, respectively. Assuming a constant velocity through the tube, we obtain from Eq. (4.3) for θ_d the expression

$$\cos \theta_d = \frac{1}{2\pi r \gamma} \left[\frac{d(mv)_{CV}}{dt} - \frac{1}{2} \rho_f \pi r^2 v^2 + 8\pi \mu (h + h_+) v + \rho_f \pi r^2 g h \right]. \quad (4.4)$$

This equation can be used to determine θ_d from the simulated $h(t)$. Notice that this is the correct form for Eq. (8) in Ref. [V]. However, the results remain almost unchanged, especially at long times, because the rise velocity is very small. By including a dynamic contact angle, determined using Eq. (4.4), in Eq. (4.1) [V], an excellent agreement was found for large r up to the latest data points, the deviation there resulting from an increase in the interface velocity close to the end of the tube.

We found good agreement with the Washburn equation also when we varied adhesion and gravity in the simulations [V]. The adhesive force defined by

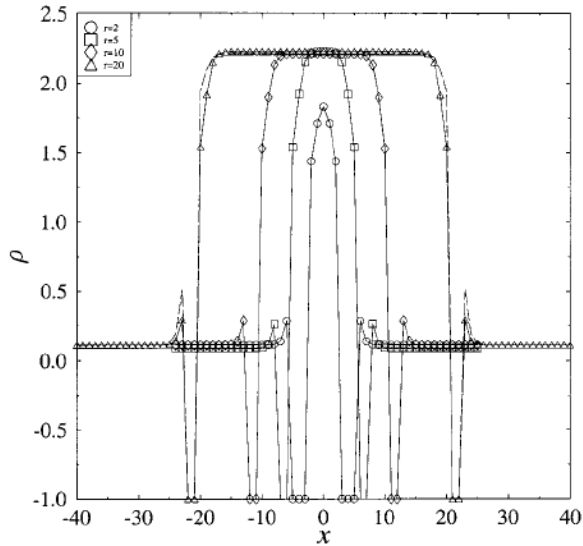


FIGURE 4.4 The density profile across the capillary tube for a radius of 2, 5, 10 and 20 lattice units. The dashed line for $r = 20$ shows the profile for stronger adhesion. A negative value of density indicates the tube wall.

Eq. (2.110) and the cohesive force defined by Eq. (2.109) both act on neighbouring fluid nodes of the solid surface. This means that the fluid-particle distribution on that node is redistributed according to the resultant of these forces. If these two competing forces were in balance, the liquid density on the node near to the solid surface would be the bulk density. Unfortunately, this is not the situation in practical simulations because, *e.g.*, it may be necessary to vary the contact angle by changing the adhesion parameter W . This is called the boundary effect.

As a result, for $r = 2$ we did not actually observe bulk liquid density inside the tube at all, as seen in the density profiles of Fig. 4.4 (here $W = -0.10$). On the outer surface of the tube, the density of the vapour was slightly higher than the bulk density of the vapour. Here capillary rise was linear in time, and also capillary condensation was seen. So, the value $r = 2$ is clearly too small for any sensible result. Inside the tube, the decay of density close to the wall was similar for $r = 5, 10, 20$, and the proportion of liquid with bulk density decreased with decreasing radius. With increasing adhesion the density of the fluid at the wall increased, *e.g.*, from 1.5 to 2.0 in the first layer for W changing from -0.10 to -0.12 , but the range of the boundary effect in the density was the same [V]. The dynamic viscosity of the liquid is not constant throughout the tube because of the density variation near the wall, *i.e.*, wall friction is a function of the adhesive force. This causes an error, which is evident from Fig. 4.5, where we show the velocity profile of a steady flow of the liquid in its equilibrium density between two infinite (by using periodic boundary conditions in the flow direction) parallel plates. There is no phase separation in our two-phase simulations here, and the flow is produced by a constant body force. For

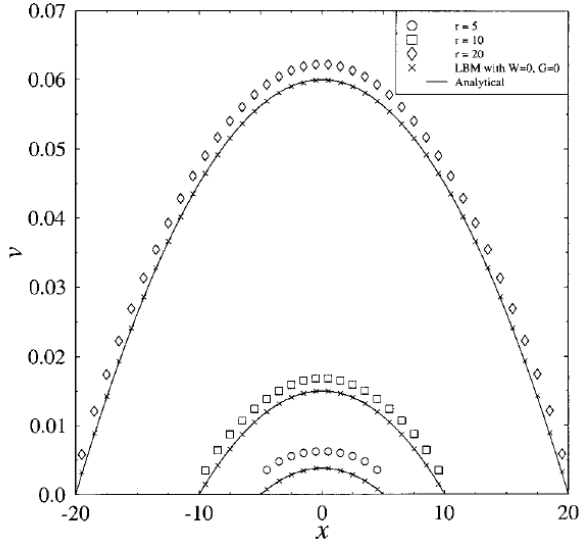


FIGURE 4.5 A typical example of the velocity profile of a fully developed flow of liquid between two parallel plates: Open symbols show our simulation results for $W = -0.1$, $G = -0.15$, $g = 0$, and the full curves denote the analytical expressions. For comparison we also show by crosses simulation data for the single-phase model with $W = G = g = 0$.

comparison, we also show in Fig. 4.5 the same result for the single-phase model. A comparison with the well-known analytical results (denoted by full curves in Fig. 4.5) shows that the velocity profile has the correct (Poiseuille) parabolic shape, but is shifted. As expected, the relative deviation decreases for increasing r . For stronger adhesion the simulated velocity profile approaches the theoretical curve and boundary effects in the density profile decrease.

The results above indicate that the general physical background of multiphase flows is included in the local interaction model except for a less accurate wall friction. This discrepancy can be almost eliminated by forcing the viscosity of the fluid to be constant by changing the relaxation parameter ξ locally as a function of density [86].

Thus, further work is needed to develop a physically more correct interaction function between the solid and fluid phases.

4.2 Simulation results

The behaviour of liquid droplets impacted on a porous medium can be roughly divided into two phases. The first phase is composed of simple spreading of a droplet over the surface, which is usually called the mechanical phase. The second phase involves penetration of the liquid into the porous medium. This phase is more difficult to analyse due to the highly complicated mechanisms of the liquid-solid interactions. The most significant mechanism is the capillary effect, which includes

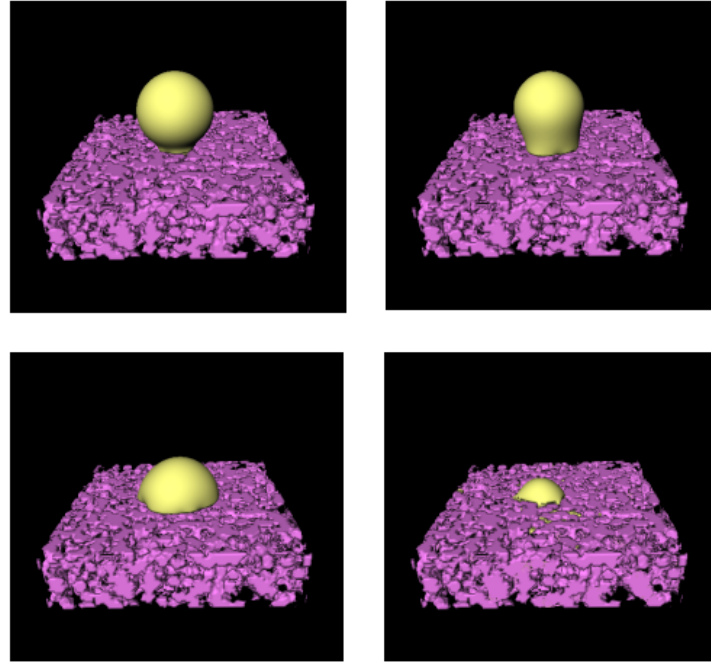


FIGURE 4.6 Absorption of a droplet into a porous medium.

also adhesion and all other chemical interactions between the liquid and the porous medium. For this reason the second phase has been called the capillary phase. In practice, these two phases are usually mixed, and penetration of the liquid already begins during the mechanical phase.

We have simulated a liquid droplet impacting, spreading and penetrating a porous medium. Visualised examples of the simulations are shown in Figs. 4.6 and 4.7. These figures show clearly how inhomogeneous the actual penetration process is. Variations in the spreading and absorption of individual droplets depend on the ratio of droplet radius to the scale of inhomogeneities in the porous surface. In order to find these variations it would be necessary to simulate the same system for several droplet sizes. So far we have done the simulation only once due to the high computational requirements. Although we now have poor statistics and the wall friction is not accurate, we still believe that the results are indicative of the true behaviour at least on a qualitative level. In the following we present some of these preliminary results.

The total simulation domain was $300 \times 300 \times 300$ lattice units and the droplet radius was $R \approx 67$. The porous medium was modelled by randomly placed and orientated, freely penetrating disks, with a radius of 10 lattice units, and with a height of 5 lattice units (see Fig. 4.8). The parameter G , which defines in addition to the surface tension also the density ratio between the liquid and the gas, was kept constant at $G = -0.15$. The relaxation parameter was $\xi = 1.0$, *i.e.*, viscosity was also constant. In Figs. 4.9 and 4.10 the wetted area is shown as a function of the

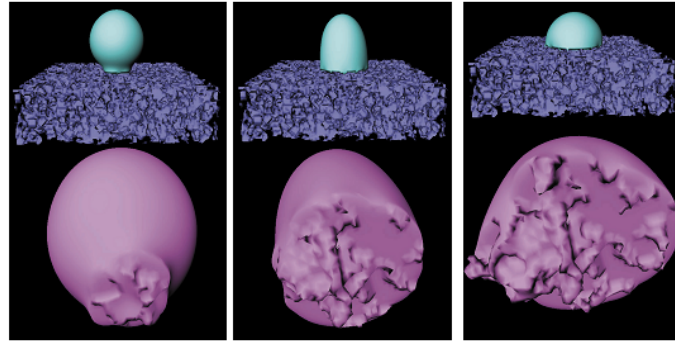


FIGURE 4.7 A view from the bottom of the droplet.

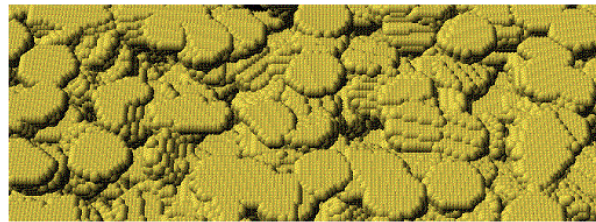


FIGURE 4.8 A modelled porous medium.

simulation time. The wetted area, which was measured along the second layer of lattice sites above the surface (the first layer is not good for this purpose because of condensation), was expressed in terms of the initial cross-section of the droplet A_0 . We simulated the spreading process for two impact velocities ($v = 0.025$ and 0.1 in lattice units), for three porosities ($\phi = 10\%$, 15% and 20%), and for two contact angles ($\theta \approx 80^\circ$ and 50° with $W = -0.10$ and -0.11 , respectively). During the mechanical

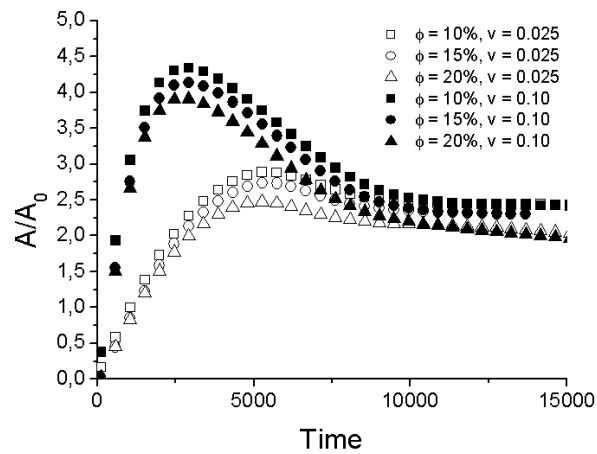


FIGURE 4.9 The wetted area as a function of simulation time for two different impact velocities, and for three different porosities. The contact angle is $\theta \approx 80^\circ$.

phase the droplet spreads on the surface due to capillary forces (adhesion between

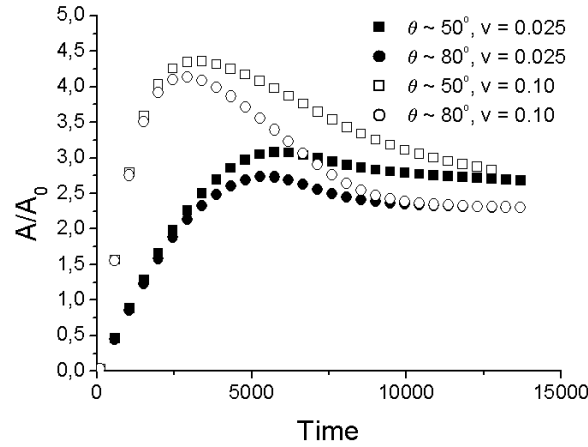


FIGURE 4.10 The wetted area as a function of simulation time for two different impact velocities, and for two different contact angles. Porosity is $\phi = 15\%$.

the solid and the liquid, surface tension of the liquid) and the kinetic energy of the droplet. When the steady-state radius is reached at the end of the mechanical phase, there is an overshoot of A/A_0 due to inertia.

At least the following conclusions can be made from our simulations of the mechanical phase: An increasing contact angle decreases the wetted area, but the impact velocity does not seem to have an effect on it (this can be seen, *e.g.*, from Fig. 4.9). Evidently penetration of the liquid into the substrate occurs very little during the mechanical phase, and the liquid on top of the substrate behaves then like a droplet whose surface energy is minimized, while dissipation consumes the impact energy. Contact angle controls also the duration of the mechanical phase. An important feature of the system is surface roughness (or porosity). Roughness causes mechanical pinning and trapping (see Fig. 4.11) of the droplet, but also makes the dynamical contact angle to fluctuate. For an increasing surface roughness (porosity), the wetted area becomes smaller (see Fig. 4.9).

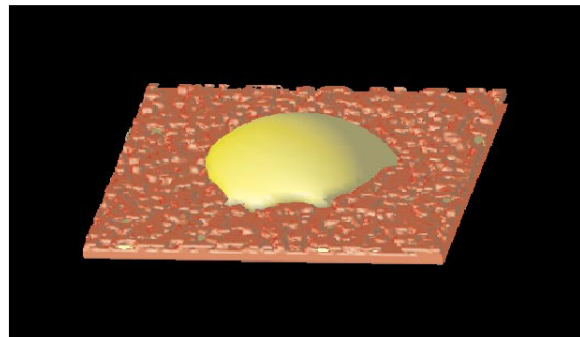


FIGURE 4.11 A late-time configuration of a spreading droplet on a rough surface.

The capillary phase begins when the droplet has established good contact with

the porous surface. (This can clearly be seen from Fig. 4.7.) The structure of the porous medium has a significant effect on the absorption of the droplet during the capillary phase, but it is difficult to precisely characterise the structure of the porous medium due to its inhomogeneity. However, one important parameter is the porosity. The effect of porosity on the absorption can be seen from Fig. 4.12, where we show the penetrated volume V of the droplet (in proportion to the initial volume) as a function of simulation time t for several different porosities and impact velocities. Adhesion plays an important role also during the capillary phase. Chemical

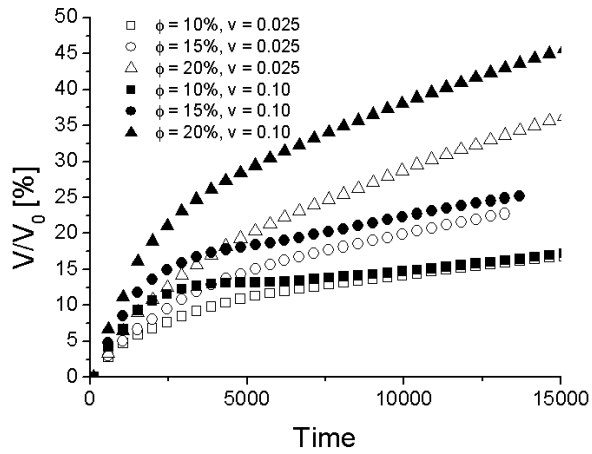


FIGURE 4.12 Penetrated volume of the droplet as a function of time for two different impact velocities, and for three different porosities.

interaction between the liquid and the porous medium is reflected in the (dynamic) contact angle. As can be seen from Fig. 4.13, absorption rate will be increased for decreasing contact angle (increasing wettability).

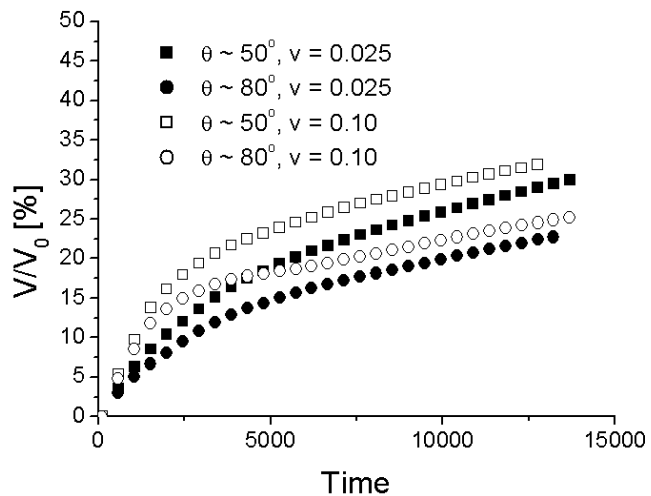


FIGURE 4.13 Penetrated volume of the droplet as a function of time for two different impact velocities, and for two different contact angles. Porosity is $\phi = 15\%$.

Impact velocity defines the initial level of the penetrated volume in the beginning of the capillary phase. The amount of penetrated fluid due to inertia becomes more significant at higher porosities (see Fig. 4.12).

By fitting a power law $V \propto t^n$ to the data, we found that the value of exponent n was close to unity in the mechanical phase, and varied in the range 0.35-0.52 in the capillary phase. These latter values are quite close to the value 0.5 (given by the Washburn equation). This indicates that there were not so much radial penetration in the porous medium which was consistent with the observations.

Finally we have simulated droplet penetration into a real three-dimensional geometry of a paper sample [87] (a hand sheet with basis weight 300 gm^{-2}). The image was made by using the X-ray tomography technique. An example of such an image of paper is shown in Fig. 4.14. X-ray microtomography is a novel technique used in three-dimensional imaging of materials [88]. This method consists of obtaining a large set of images while passing radiation through the sample at different angles. The projected images can be combined so as to reconstruct the geometry of the interior structure.

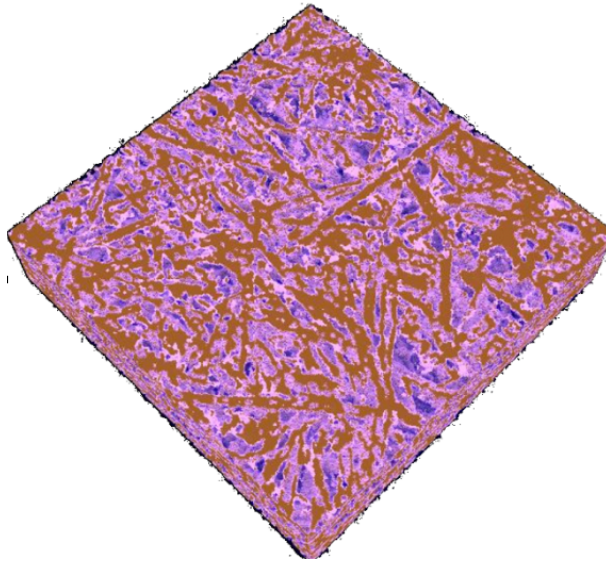


FIGURE 4.14 A tomographic image of paper. Side length is 0.8 mm , and resolution $2\text{ }\mu\text{m}$.

The size of the sample used in the simulation was $300 \times 300 \times 100$ lattice units whereas the size of the whole simulation domain was $300 \times 300 \times 260$ lattice units, including a droplet with an initial diameter of about 95 lattice units. The surface tension and adhesion were controlled by setting $G = -0.15$ and $W = -0.10$. The impact velocity of the droplet was zero, and the relaxation-time parameter was $\xi = 1.0$. Figure 4.15 shows the droplet at six different stages of penetration. To analyse the penetration kinetics we measured the basal radius and volume of the droplet above the sample surface as a function of time. In spite of the fact that the droplet

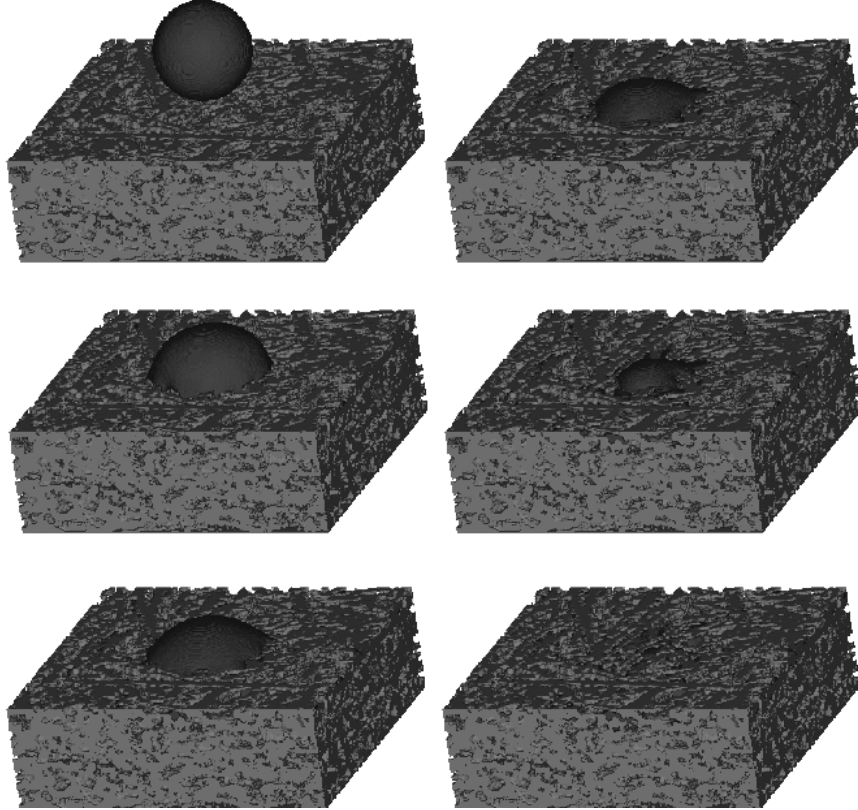


FIGURE 4.15 Snapshots of droplet penetration into paper.

penetrates not only in the in-plane directions but also in the transverse direction through the course of the simulation, we found that liquid mostly stayed close to the sample surface. In other words, penetration in the transverse direction was much slower than in the in-plane direction. This means that the assumption of purely two-dimensional penetration in the vicinity of paper surface is not at all unreasonable. In order to better understand these simulation results, we constructed a model for radial capillary penetration.

Our model is based on the assumption that radial capillary penetration can be described as penetration in cylindrical capillary tubes. We also assume that liquid flow in such tubes is laminar and fully developed, and that inertial effects can be neglected. Under these assumptions the pressure drop due to viscous drag in a tube of radius a is

$$\frac{dP}{dl} = -\frac{8\mu v}{a^2}, \quad (4.5)$$

where v is the average velocity of the liquid. Now, at distance l from the centreline of the source, velocity v can be written in terms of volumetric flow Q such that

$$v = \frac{dl}{dt} = \frac{Q}{2\pi l H \phi}, \quad (4.6)$$

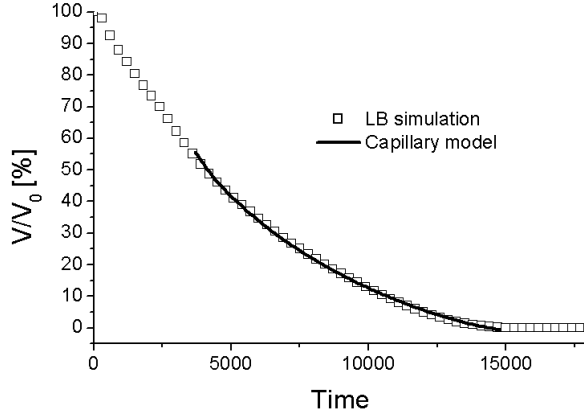


FIGURE 4.16 Volume of a droplet on the surface of the paper sample as a function of time. The solid line is the result of a numerical integration of Eq. (4.9). Integration was applied after the mechanical phase of droplet spreading.

where H is the height and ϕ the porosity of the sample. By inserting Eq. (4.6) into Eq. (4.5), the pressure drop in the sample can be expressed in the form

$$\frac{dP}{dl} = -\frac{4\mu Q}{\pi a^2 H \phi} \frac{1}{l}. \quad (4.7)$$

Under the assumption of incompressible liquid, Q does not depend on l . Therefore Eq. (4.7) can be integrated from the interface of the source ($l = R_0$) up to the liquid-gas interface ($l = R$), and we find that

$$P(R_0) - P(R) = \frac{4\mu Q}{\pi a^2 H \phi} \ln \frac{R}{R_0}, \quad (4.8)$$

where the left-hand side also equals the capillary pressure $P_c = 2\gamma \cos \theta/a$. After using this relation, and with the help of Eq. (4.6), we obtain

$$4R \ln \left(\frac{R}{R_0} \right) \frac{dR}{dt} = \frac{a\gamma \cos \theta}{\mu}. \quad (4.9)$$

The simulated result can now be compared with the one obtained by integrating Eq. (4.9) numerically. The result of this comparison is shown in Fig. (4.16). In the present case R_0 is the basal radius of the droplet and is thus a function of time. Although the size of the droplet is small compared to the scale of inhomogeneities in the paper, and our capillary model assumes an infinite liquid reservoir, an excellent agreement between the capillary model and the lattice-Boltzmann simulation is observed. (We also performed experiments in which we put single water droplets ($a \approx 0.7 \text{ mm}$) on the surface of a porous medium ($H \approx 15 \mu\text{m}$, $\phi \approx 10\%$). By using two CCD cameras we were able to measure the penetrated volume of the droplet. The agreement between these experimental results and the results obtained from Eq. (4.9) was rather

good.) In our study of a single capillary tube [V] we found some inaccuracy in the interaction between the solid and liquid phases, especially for a small radius of the capillary tube. However, as evidenced by our penetration results, even in a sample with quite small pores realistic results can be obtained, even though the behaviour in single small pores might be inaccurate [87]. This is most probably due to the fact that the smallest pores do not give a detectable contribution to the penetration process.

Chapter 5

Conclusions

We have used the lattice-Boltzmann method to investigate the behaviour of non-Brownian liquid-particle suspensions as a function of variables such as the concentration and shape of the suspended particles, and the shear rate. For increasing shear rate we found that suspensions display shear thickening *i.e.* their apparent viscosity increases with increasing shear Reynolds numbers. We also observed that shear thickening is related to enhanced relative solid-phase momentum transfer. This enhancement in the momentum transfer can arise at least from two mechanisms: deformation of suspension microstructure (clustering) for $Re_\gamma \lesssim 1$, and inertial effects for $Re_\gamma > 1$. In shear flow suspended particles form dynamic linear clusters which rotate and effectively transfer momentum across the system before disappearing. We found that the viscosity of the suspension correlates with the cluster size for Reynolds numbers $Re_\gamma \lesssim 1$. For high particle Reynolds numbers $Re_\gamma > 1$ when the cluster size remains almost constant, the viscosity increases due to inertial effects.

We also analysed the behaviour of a liquid droplet on a porous surface by 3D lattice-Boltzmann simulations. Our preliminary results indicate that we can qualitatively understand how the impact velocity of the droplet, contact angle and pore geometry affect the evolution of the wetted area. Penetration of a liquid droplet into a tomographic image of a sample of paper was as well consired. We determined the volume penetrated by the droplet as a function of time, and compared it with the corresponding result of an analytical capillary model. We could conclude that, even for a sample with quite small pores, realistic results could be obtained although the simulated behaviour in single small pores might not have been very realistic because of pronounced discretization effects.

It is evident that the lattice-Boltzmann method is a convenient tool for analysing the behaviour of multiphase flows. We believe that the results already obtained will help to better understand the rheological behaviour of multiphase flows which appear in numerous applications that range from blood flow to industrial processes.

Bibliography

- [I] P. Raiskinmäki, A. Shakib-Manesh, A. Koponen, A. Jäsberg, M. Kataja, and J. Timonen, *Comput. Phys. Commun.* **129**, 185 (2000).
- [II] A. Shakib-Manesh, P. Raiskinmäki, A. Koponen, M. Kataja, and J. Timonen, *J. Stat. Phys.* **107**, 67 (2002).
- [III] P. Raiskinmäki, J. A. Åström, M. Kataja, M. Latva-Kokko, A. Koponen, A. Jäsberg, A. Shakib-Manesh and J. Timonen, *Phys. Rev. E* **68** (2003) 061403
- [IV] P. Raiskinmäki, A. Koponen, J. Merikoski, and J. Timonen, *Comput. Mat. Sci.* **18** (1), 7 (2000).
- [V] P. Raiskinmäki, A. Shakib-Manesh, A. Koponen, A. Jäsberg, J. Merikoski, and J. Timonen, *J. Stat. Phys.* **107**, 143 (2002).
- [1] K. Huang, *Statistical mechanics* (New York, 1967).
- [2] P.L. Bhatnagar, E.P. Gross, and M. Krook, *Phys. Rev.* **94**, 511 (1954).
- [3] F.M. White, *Fluid mechanics* (New York, 1994).
- [4] S.L. Soo, *Multiphase Fluid Dynamics* (Science Press, Beijing, 1990).
- [5] D.A. Drew, *Ann. Rev. Fluid Mech.* **15**, 261 (1983).
- [6] D.A. Drew, *Arch. Rat. Mech. Anal.* **62**, 117 (1976).
- [7] D.A. Drew and R.T. Lahey, *Int. J. Multiphase flow*, **5**, 243 (1979).
- [8] A. Jäsberg, A. Koponen, M. Kataja, and J. Timonen, *Comput. Phys. Commun.* **129**, 196 (2000).
- [9] M. Manninen, V. Taivassalo, and S. Kallio, Research report 288, VTT Technical Research Centre of Finland, Espoo, (1996).
- [10] A. Einstein, *Ann. Physik*, **19**, 289 (1906); A. Einstein, *Ann. Physik*, **34**, 591 (1911).
- [11] G.K. Batchelor, *J. Fluid Mech.* **83**, 97 (1977).

- [12] I.M. Krieger and T.J. Dougherty, *Trans. Soc. Rheol.* **3**, 137 (1959).
- [13] H.A. Barnes, J.F. Hutton, and K. Walters, *An introduction to Rheology* (Amsterdam, 1993).
- [14] R.L. Hoffman, *J. Rheol.* **42**, 111 (1998).
- [15] T. Phung and J.F. Brady, *Slow dynamics in Condensed Matter* edited by K. Kawasaki, M. Tokuyama, and T. Kawakatsu (AIP, Woodbury, NY, 1992), **256**, 391.
- [16] G. Bossis and J.F. Brady, *J. Chem. Phys.* **91**, 1866 (1989).
- [17] J.F. Brady and G. Bossis, *Annu. Rev. Fluid Mech.* **20**, 111 (1988).
- [18] U. Frisch, B. Hasslacher, and Y. Pomeau, *Phys. Rev. Lett.* **56**, 1505 (1986).
- [19] G.R. McNamara and G. Zanetti, *Phys. Rev. Lett.* **61**, 2332 (1988).
- [20] P.J. Hoogerbrugge and J.M.V.A. Koelman, *Europhys. Lett.* **19**, 155 (1992).
- [21] E.S. Boek, P.V. Coveney, H.N.W. Lekkerkerker, and P. van der Schoot, *Phys. Rev. E* **55**, 3124 (1997).
- [22] R. Benzi, S. Succi, and M. Vergassola, *Phys. Rap.* **222**, 145 (1992).
- [23] S. Chen and G.D. Doolen, *Annu. Rev. Fluid Mech.* **30**, 329 (1998).
- [24] D.H. Rothman and S. Zaleski, *Lattice-gas cellural automata; Simple models of complex hydrodynamics* (Cambridge University Press, 1997).
- [25] A. Koponen, PhD thesis, University of Jyväskylä, (Jyväskylä, Finland, 1998).
- [26] Y.H. Qian, D. d'Humières, and P. Lallemand, *Europhys. Lett.* **17**, 479 (1992).
- [27] O. Behrend, R. Harris, and P.B. Warren, *Phys. Rev. E* **50**, 4586 (1994).
- [28] J.D. Sterling and S.Y. Chen, *J. Comput. Phys.* **123**, 196 (1996).
- [29] T. Abe, *J. Comput. Phys.* **131**, 241 (1997).
- [30] X.Y. He and L.S. Luo, *Phys. Rev. E* **55**, R6333 (1997).
- [31] B. Chopard and M. Drotz, *Cellular automata modelling of physical systems* (Lecture notes, University of Geneva, 1996).
- [32] M. Gallivan, D. Noble, J. Georgiadis, and R. Bockius, *Int. J. Numer. Meth. Fluids*, **25**, 249 (1997).

- [33] D. Kandhai, A. Koponen, A. Hoekstra, M. Kataja, J. Timonen, and P. Sloot, *J. Comp. Phys.* **150**, 482 (1999).
- [34] A.J.C. Ladd and R. Verberg, *J. Stat. Phys.* **104**, 1191 (2001).
- [35] A.J.C. Ladd, *J. Fluid Mech.* **271**, 285 (1994).
- [36] P.A. Skordos, *Phys. Rev. E* **486**, 4823 (1993).
- [37] D.R. Noble, S. Chen, J.G. Georgiadis, and R.O. Buckius, *Phys. Fluids*, **7 1**, 203 (1995).
- [38] B. Ferréol and D.H. Rothmann, *Transport in Porous Media*, **20**, 3 (1995).
- [39] A.J.C. Ladd, *J. Fluid Mech.* **271**, 311 (1994).
- [40] O. Behrend, *Phys. Rev. E* **52**, 1164 (1995).
- [41] C.K. Aidun and Y.N. Lu, *J. Stat. Phys.* **81**, 49 (1995).
- [42] D. Kandhai, A. Koponen, A. Hoekstra, M. Kataja, J. Timonen, and P. Sloot, *Comput. Phys. Commun.* **111**, 14 (1998).
- [43] C.K. Aidun, Y.N. Lu, and E. Ding, *J. Fluid. Mech.* **373**, 287 (1998).
- [44] R. Verberg and A.J.C. Ladd, *Phys. Rev. Lett.* **84**, 2148 (2000).
- [45] P. Lallemand and L-S. Luo, *J. Comput. Phys.* **184**, 406 (2003).
- [46] E. Aurell and M. Do-Quang, ePrint, <http://xxx.lanl.gov/abs/cond-mat/0105372>, (2001).
- [47] A.K. Gunstensen, D.H. Rothman, S. Zaleski, and G. Zanetti, *Phys. Rev. A* **43**, 4320 (1991).
- [48] D.H. Rothman and J.M. Keller, *J. Stat. Phys.* **52**, 1119 (1988).
- [49] D. Grunau, S.Y. Chen, and K. Eggert, *Phys. Fluids A* **5**, 2557 (1993).
- [50] E.G. Flekkøy, *Phys. Rev. E* **47**, 4247 (1993).
- [51] A.K. Gunstensen and D.H. Rothman, *J. Geophysical Res.* **98**, 6431 (1993).
- [52] I. Halliday, C.M. Care, S. Thompson, and D. White, *Phys. Rev. E* **54**, 2573 (1996).
- [53] Y. Kato, K. Kono, T. Seta, et al, *Int. J. Modern. Phys. C* **8**, 843 (1997).
- [54] X. Nie, Y. Qian, S. Chen, and G.D. Doolen, *Phys. Rev. E* **58**, 6861 (1998).
- [55] X. Shan and H. Chen, *Phys. Rev. E* **47**, 1815 (1993).

- [56] X. Shan and H. Chen, Phys. Rev. E **49**, 2941 (1994).
- [57] N.S. Martys and H. Chen, Phys. Rev. E **53**, 743 (1996).
- [58] J. Hyväläluoma, P. Raiskinmäki, A. Jäsberg, A. Koponen, M. Kataja and J. Timonen, Future Gen. Comput. Systems, **20**, 1003 (2004).
- [59] X. Shan and G. Doolen, J. Stat. Phys. **81**, 379 (1995).
- [60] L.-S. Luo, Phys. Rev. E **62** 4, 4982 (2000).
- [61] Z.L. Yang, T.N. Dinh, R.R. Nourgaliev, and B.R. Sehgal, Heat and Mass Transfer, **36**, 295 (2000).
- [62] M. Schelkle and A. Frohn, J. Aerosol Sci. **26** (1), S145 (1995).
- [63] Z.L. Yang, T.N. Dinh, R.R. Nourgaliev, and B.R. Sehgal, Int. J. Heat and Mass Transfer, **44**, 195 (2001).
- [64] Z.L. Yang, B. Palm, and B.R. Sehgal, Int. J. Heat and Mass Transfer, **45**, 631 (2002).
- [65] M.R. Swift, W.R. Osborn, and J.M. Yeomans, Phys. Rev. Lett. **75**, 830 (1995).
- [66] M.R. Swift, E. Orlandini, W.R. Osborn, and J.M. Yeomans, Phys. Rev. E **54**, 5041 (1996).
- [67] B.T. Nadiga and S. Zaleski, Eur. J. Mech. B/Fluids, **15**, 885 (1996).
- [68] D.J. Holdych, D. Rovas, J.G. Georgiadis, and R.O. Buckius, Int. J. Mod. Phys. C **9**, 1393 (1998).
- [69] G. Gonnella, E. Orlandini, and J.M. Yeomans, Phys. Rev. Lett. **78**, 1695 (1997).
- [70] A.J. Wagner and J.M. Yeomans, Phys. Rev. Lett. **80**, 1429 (1998).
- [71] A.J. Wagner and J.M. Yeomans, Int. J. Mod. Phys. C **8**, 773 (1997).
- [72] J.M. Buick and C. A. Created, Phys. Fluids, **10**, 1490 (1998).
- [73] X.Y. He, X.W. Shan, and G.D. Doolen, Phys. Rev. E **57**, R13 (1998).
- [74] X.Y. He, S. Chen, and R. Zhang, J. Comput. Phys. **152** 2, 642 (1999).
- [75] S. Chapman and T.G. Cowling, *The mathematical theory of non-uniform gases*, 3rd ed. (Cambridge University Press, Cambridge, 1970).
- [76] T.L. Dodd, D.A. Hammer, A.S. Sangani, and D.L. Koch, J. Fluid Mech. **293**, 147 (1995).

- [77] J. Feng, H.H. Hu, and D.D. Joseph, *J. Fluid Mech.* **353**, 1 (1997).
- [78] A. Miyamura, S. Iwasaki, and T. Ishii, *Int. J. Multiphase Flow*, **7**, 41 (1981).
- [79] J. C. van der Werff and C. G. de Kruif, *J. Rheol.* **33**, 421 (1989).
- [80] J. F. Brady, *J. Chem. Phys.* **99**, 567 (1993).
- [81] T. Kemppinen and M. Toivakka, to be published.
- [82] R.S. Farr, J.R. Melrose, and R.C. Ball, *Phys. Rev. E* **55**, 55 (1997).
- [83] L. H. Tanner, *J. Phys. D* **12**, 1473 (1979).
- [84] J. Hyväläluoma, P. Raiskinmäki, A. Koponen, M. Kataja and J. Timonen, Submitted to *Computers & Fluids*.
- [85] E. W. Washburn, *Phys. Rev.* **17**, 273 (1921).
- [86] J. Hyväläluoma, P. Raiskinmäki, A. Koponen, M. Kataja, and J. Timonen, to be published.
- [87] J. Hyväläluoma, P. Raiskinmäki, A. Jäsberg, A. Koponen, M. Kataja, J. Timonen, and S. Ramaswamy to be published.
- [88] A. Goel, M. Tzanankakis, S. Huang, S. Ramaswamy, D. Choi, and B. V. Rama-rao, *Tappi J.* **84**, 1 (2001).